

Detection of delayed target response in SAR

Mikhail Gilman[✉] and Semyon Tsynkov

Department of Mathematics, North Carolina State University, Campus Box 8205,
Raleigh, NC 27695, United States of America

E-mail: mgilman@ncsu.edu

Received 11 December 2018, revised 5 April 2019

Accepted for publication 25 April 2019

Published 30 July 2019



CrossMark

Abstract

Delayed target response in synthetic aperture radar (SAR) imaging can be obscured by the range-delay ambiguity and speckle. To analyze the range-delay ambiguity, one extends the standard SAR formulation and allows both the target reflectivity and the image to depend not only on the coordinates, but also on the response delay. However, this still leaves the speckle unaccounted for. Yet speckle is commonly found in SAR images of extended targets, and a statistical approach is usually employed to describe it. We have developed a simple model of a delayed scatterer by modifying the random function that describes a homogeneous extended scatterer. Our model allows us to obtain a relation between the deterministic parameters of the target model and statistical moments of the SAR image. We assume a regular shape of the antenna trajectory, and our model targets are localized in at least one space-time coordinate; this permits analytical formulation for statistical moments of the image. The problem of reconstruction of coordinate-delay reflectivity function is reduced to that of discrimination between instantaneous and delayed scatterers; for the latter problem, the maximum likelihood based image processing procedure has been developed. We perform Monte-Carlo simulation and evaluate performance of the classification procedure for a simple dependence of scatterer reflectivity on the delay time.

Keywords: delayed scattering, dispersive targets, synthetic aperture radar, speckle, range-delay ambiguity

(Some figures may appear in colour only in the online journal)

1. Introduction

Detection of targets with delayed response, or the so-called dispersive targets, can provide valuable information for the interpretation of the observed scene in synthetic aperture radar (SAR) imaging. Man-made objects often exhibit delayed response, and the characteristics of reflectivity in the ‘delay’ coordinate depend on the scale, internal structure, and material of the target [1–6].

Two major obstacles to retrieving the delay information from radar signals are the range-delay ambiguity and speckle. Radar images are built by processing the signals that have been emitted by the radar antenna, scattered by a target, and then received by either the same or a different antenna. The received signal is a function of time, which is a single scalar variable. The central assumption of the signal processing algorithms (i.e. the algorithms that convert the signal into an image, which is a function of two target coordinates) is that the travel time of a signal is proportional to the travel distance, given that the propagation speed is constant. This relation no longer holds if reflection at the target involves some delay. When this delay exceeds the travel time between the adjacent image pixels, the delayed return contributes to the instantaneous returns from the pixels at larger distances from the antenna compared to the pixel containing the delayed target. Hence, objects with delayed return will appear in the images as streaks in the range direction. When there is only one radar signal involved, there is no possibility to distinguish, without additional information, between the delayed response from an object and an immediate return from another object at a larger distance.

The range-delay ambiguity can, in principle, be resolved if we consider the reflection of multiple signals that impinge on the target from different directions, as done in SAR imaging. Indeed, the distance between the antenna and various parts of the target is a function of the observation angle. At the same time, the delayed response is typically determined by the internal composition and/or geometry of the target and does not depend on the observation angle. This difference in the properties of the two types of reflected signals is exploited in [6] for building a model for SAR imaging of the targets with the reflectivity function that varies in space and may also involve a delayed component.

The resulting procedure, however, appears to have insufficient sensitivity and low resolution in the delay variable. For narrow and moderate apertures, which are the most popular SAR acquisition modes, the range-delay ambiguity is not very well resolved. Additionally, the speckle effect [7, 8], which is common in SAR images, complicates the detection of small variations of image intensity [9]. This effect is often described in statistical framework where the image pixels are random variables with certain probability distributions. Hence, individual pixel values in the image are not a reliable source of information about the target reflectivity as a function of the coordinates and delay. In other words, if the difference between the images of two deterministic targets, instantaneous and delayed, is small in the first place, then, on a random background due to speckle, these targets may become indistinguishable.

In this work, we address the challenges due to the presence of speckle and range-delay ambiguity by means of accumulating and processing the redundant data. In particular, we adopt a statistical approach for the description of the scattering process and imaging and use multiple delay measurements in order to mitigate the stochastic effects. We propose an ‘incoherent’ scatterer model, which is an extension of the commonly used concept of ‘uniform delta-correlated background’, to describe different scatterer types, including those with delayed response. Whereas the standard objective for SAR is to reconstruct the scattering characteristics of the target, our aim is rather to detect a delayed return immersed into an instantaneous background. This can be thought of as ‘lowering the bar’ for the output of the inverse problem as compared to [6]. The gain here is that our approach helps increase the

robustness of discrimination between instantaneous and delayed targets. We will see, however, that an unfavorable combination of the target and system parameters can still make a reliable discrimination impossible. Accordingly, we will assess the performance of our procedure by the percentage of incorrect discriminations between different scene types.

The literature on conventional SAR is substantial, see, e.g. [10, 11], as well as [12, chapter 2]. An extensive review on SAR imaging of non-instantaneous targets can be found in the recent article [6]. The specific approach proposed in [6] for handling the delayed returns is based on the coordinate-delay imaging operator (see section 2). An alternative to that is sub-banding, see, e.g. [3]. The latter technique involves splitting the available bandwidth into several sub-bands and building individual SAR images in each sub-band. This, of course, decreases the resolution of the entire image. Besides, long and gradual response delays, such as the one due to a cavity in [6], have a very narrow manifestation in the frequency domain. Hence, sub-banding may remain inefficient until the resolution becomes as low as the streak length. Another class of approaches, see [13] and [1, chapter 4], have the delayed response parametrized by means of a sum of several fixed-frequency waveforms followed by either spectral filtering or an optimization procedure. This method should work well if the delayed return is highly coherent, i.e. concentrated in a few waveforms, each having a bandwidth much smaller than that of the signal. The effect of speckle is not accounted for in either [13] or [1, chapter 4] though.

Similarly to [6], we adopt the linearized scattering model based on the first Born approximation. Linearization is critical for the quantitative analysis of SAR imaging. The first Born approximation renders linearization by assuming that the scattering is weak. This model has been, and still remains, the de-facto standard in the literature on SAR imaging even though the scattering is strong in most cases, including that by soil, sea surface, buildings, etc. In our current work, we employ the first Born approximation (as opposed to other asymptotic models, such as Kirchhoff, small-slope approximation, composite roughness, etc [14–17]) because it is capable of correctly capturing the Bragg resonant mechanism that is responsible for backscattering and can be extended to the case where the scattering remains linearized but is no longer weak, see [18] and [12, chapter 7].

The current paper starts with the analysis of the coordinate-delay imaging operator in section 2. Statistical models of the scene components, such as the background, the delayed target, and the instantaneous inhomogeneous target, are introduced in section 3. The discrimination procedure is described in section 4, while the Monte-Carlo simulation to assess the quality of discrimination is described in section 5. The results and discussion are presented in sections 6 and 7, respectively. Some technical details are provided in appendix.

2. Coordinate-delay imaging operator

2.1. Instantaneous and delayed scattering and range-delay ambiguity

In monostatic SAR imaging, multiple signals are emitted by the radar antenna, scattered about the target, and received by the same antenna. The propagation of a scalar field $u^i(t, \mathbf{z})$ due to forcing $P(t)$ at the point \mathbf{x} is described by

$$u^i(t, \mathbf{z}) = \frac{1}{4\pi R_z} P\left(t - \frac{R_z}{c}\right),$$

where $R_z = |\mathbf{z} - \mathbf{x}|$. Following [6] and [11, chapter 6], we describe the relation between the incident field u^i and scattered field u^s as convolution in time:

$$\begin{aligned}
u^s(t, \mathbf{z}) &= \int_0^\infty u^i(t - t_z, \mathbf{z}) \nu(t_z, \mathbf{z}) dt_z \\
&= \int_0^\infty \frac{1}{4\pi R_z} P\left(t - \frac{R_z}{c} - t_z\right) \nu(t_z, \mathbf{z}) dt_z.
\end{aligned} \tag{1}$$

In this formulation, the reflectivity function $\nu(t_z, \mathbf{z})$ describes the delayed response of a linear material to the incident field. The lower limit of integration in (1) is set to zero due to the causality, and the interaction of the scattered field with the target is neglected following the first Born approximation. Hereafter, we will assume that the integrals of the type that appear in (1) are finite.

For standard SAR where all the targets are instantaneous, formula (1) simplifies and the relation between the scattered and emitted field becomes:

$$u^s(t, \mathbf{z}) = \nu_{\text{inst}}(\mathbf{z}) u^i(t, \mathbf{z}) \implies \nu(t_z, \mathbf{z}) = \nu_{\text{inst}}(\mathbf{z}) \delta(t_z), \tag{2}$$

where δ is the Dirac delta function.

In this work, we take the pulse receive location to be the same as its transmit location, i.e. \mathbf{x} . Propagating the scattered signal (1) back to \mathbf{x} from all scattering locations \mathbf{z} , we obtain

$$u_x^s(t) \equiv u^s(t, \mathbf{x}) = \int_0^\infty dt_z \int d\mathbf{z} \frac{1}{16\pi^2 R_z^2} \nu(t_z, \mathbf{z}) P\left(t - \frac{2R_z}{c} - t_z\right). \tag{3}$$

In what follows, we will assume that the target is observed from the distance much larger than its size. This allows us to disregard the dependence of R_z^{-2} on \mathbf{z} and, subsequently, incorporate $\frac{1}{16\pi^2 R_z^2}$ into ν as a constant factor. Moreover, the motion of the antenna during the pulse transmission and reception causes the Doppler shift of the signal frequency; we assume that this effect can be disregarded as well (this is the so-called start-stop approximation; its validity has been explored in [12, chapter 6]).

The range-delay ambiguity is easiest to understand in the 1D case where $\mathbf{x} = x$, $\mathbf{z} \equiv z$, and $R_z = R + z$, $R = \text{const}$. Then, it appears fundamentally impossible to unambiguously reconstruct a function of two arguments $\nu(t_z, z)$ from the function of a single argument $u_x^s(t)$. Indeed, the substitution

$$\nu(t_z, z) \leftarrow \nu'(t_z, z) = \nu(t_z, z) + f\left(\frac{2R_z}{c} + t_z\right) g(t_z), \tag{4}$$

where $\int_0^\infty g(t_z) dt_z = 0$ and $f(t_z)$ is an integrable function, does not affect $u_x^s(t)$ given by (3), as one can see by changing the integration variables: $(t_z, z) \mapsto (t_z, t_z + 2z/c)$. Hence, the inversion $u_x^s(t) \mapsto \nu(t_z, z)$ cannot be unique.

A single-pulse coordinate-delay image is formed by the application of a matched filter to the received signal (see, e.g. [6]):

$$I_x(t_y, \mathbf{y}) = \int \underbrace{P\left(t - \frac{2R_y}{c} - t_y\right)}_{\text{matched filter}} u_x^s(t) dt, \tag{5}$$

where $R_y = |\mathbf{y} - \mathbf{x}|$ and the overbar means complex conjugation. Substituting (3) into (5) and changing the order of integration, we obtain a convolution expression for the image:

$$I_x(t_y, \mathbf{y}) = \int_0^\infty dt_z \int d\mathbf{z} \nu(t_z, \mathbf{z}) \underbrace{\int dt P\left(t - \frac{2R_y}{c} - t_y\right) P\left(t - \frac{2R_z}{c} - t_z\right)}_{W_x(t_y, \mathbf{y}; t_z, \mathbf{z})}. \tag{6}$$

In (6), the kernel of the transformation $\nu(t_z, \mathbf{z}) \mapsto I_x(t_y, \mathbf{y})$, or the imaging kernel, is the point spread function (PSF) $W_x(t_y, \mathbf{y}; t_z, \mathbf{z})$. Changing the integration variable in the innermost integral of (6), we can show that W_x is a function of one argument:

$$W_x(t_y, \mathbf{y}; t_z, \mathbf{z}) \equiv W_x\left(t_y - t_z + \frac{2R_y - 2R_z}{c}\right). \quad (7)$$

Hence, $I_x(t_y, \mathbf{y})$ turns out to be a function of only one argument, $(t_y + 2R_y/c)$, as well. For example,

$$I_x(t_y, \mathbf{y}) = I_x(0, \mathbf{y}') \quad \text{whenever} \quad |\mathbf{y}' - \mathbf{x}| = |\mathbf{y} - \mathbf{x}| + \frac{ct_y}{2}. \quad (8)$$

While (4) can be seen as a manifestation of the range-delay ambiguity in the target coordinates, i.e. t_z and \mathbf{z} , formula (8) describes the same effect in terms of the image coordinates t_y and \mathbf{y} .

For standard SAR and instantaneous targets, see (2), formula (6) becomes

$$I_x(\mathbf{y}) = \int d\mathbf{z} \nu_{\text{inst}}(\mathbf{z}) \underbrace{\int dt P\left(t - \frac{2R_y}{c}\right) P\left(t - \frac{2R_z}{c}\right)}_{W_x(\mathbf{y}, \mathbf{z}) \equiv W_x(R_y - R_z)}, \quad (9)$$

and the PSF no longer has the time arguments.

2.2. Coordinate-delay SAR image and the kernel of the imaging operator

The range-delay ambiguity can be resolved by interrogating the target from different antenna positions. In other words, the observation direction must span a certain sufficiently wide interval. Wide-angle SAR imaging is described, e.g. in [19]. The ultimate case of the so-called (full) circular SAR, where the observation platform makes a circle around the target during the image acquisition, is presented in [20, 21]. However, for wide-angle SAR one can no longer assume that the reflectivity does not depend on the direction, as in (1). In this work, we rather want formula (1) to hold so that ν does not depend on \mathbf{x} , a condition sometimes called angular coherence, see, e.g. [19, 22–24]. This implies that there is a dominant observation direction. On the other hand, for detecting a delayed response the span of observation angles may not be too narrow, as we will see in section 4.1, formula (64).

We take x_2 as the horizontal coordinate aligned with the dominant observation direction, x_1 normal to it and also horizontal, and x_3 vertical, as shown in figure 1. The direction x_2 will be referred to as range, and x_1 as azimuth or cross-range. The antenna trajectory at a reference distance R from the target is specified as an arc of a circle:

$$\mathbf{x} = \mathbf{x}(\varphi) = (-L \sin \varphi, -L \cos \varphi, H), \quad |\varphi| \leq \varphi_T/2, \quad (10)$$

where φ is the aspect angle and φ_T defines the synthetic aperture or, more precisely, its angular width. In addition to that, $L = R \sin \theta$ in formula (10) is the circle radius, $H = R \cos \theta$ is the platform altitude, and θ is the incidence angle, see figure 1. The coordinates associated with the target and image will be denoted by $\mathbf{z} = (z_1, z_2, z_3)$ and $\mathbf{y} = (y_1, y_2, 0)$, respectively. Moreover, the scattering will be assumed to occur only on the surface of the target, i.e. on the plane $z_3 = 0$, which is a common assumption in SAR. Hence, throughout this paper we will consider

$$\mathbf{z} = (z_1, z_2, 0) \quad \text{and} \quad \mathbf{y} = (y_1, y_2, 0). \quad (11)$$

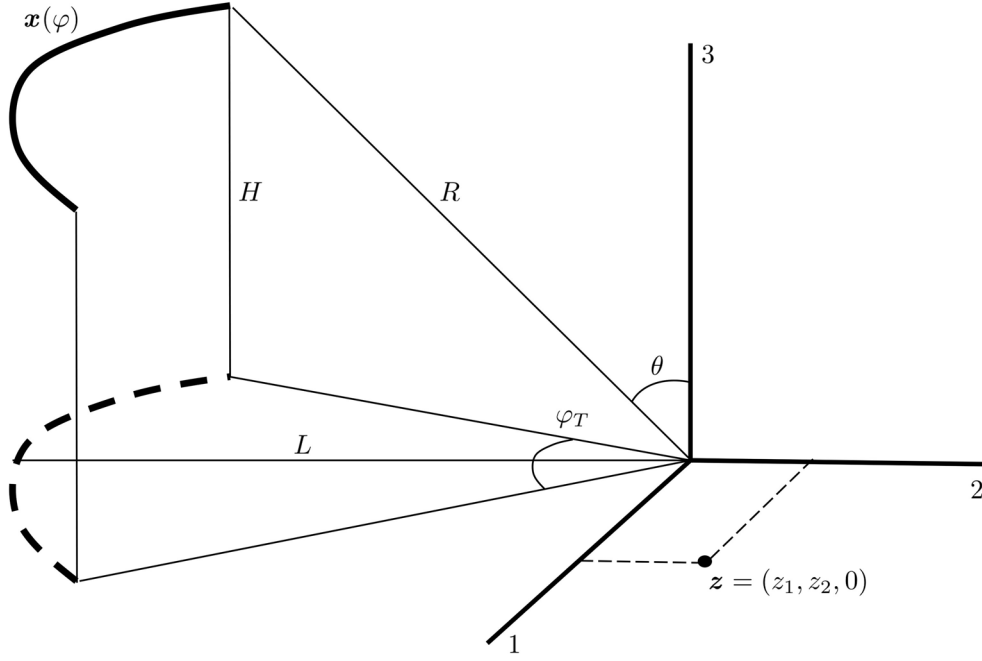


Figure 1. Geometry of the problem.

Accordingly, the reflectivities ν and ν_{inst} , see (1) and (2), will depend only on two spatial coordinates (see [18] and [12, chapter 7] for additional detail).

We will not consider either very steep or very shallow incidence, which implies $\sin \theta = \mathcal{O}(1)$ and $\cos \theta = \mathcal{O}(1)$. The presence of a dominant observation direction requires $\varphi_T \ll 1$. For $R_z^\varphi \stackrel{\text{def}}{=} |\mathbf{z} - \mathbf{x}(\varphi)|$ we have:

$$R_z^\varphi = (R^2 + z_1^2 + z_2^2 + 2L(z_1 \sin \varphi + z_2 \cos \varphi))^{1/2}.$$

Assuming that the entire target area of interest is near the origin of the coordinate system, $|\mathbf{y}|, |\mathbf{z}| \ll R$ (see figure 1), we simplify the previous expression as follows:

$$R_z^\varphi \approx R + \sin \theta (z_1 \sin \varphi + z_2 \cos \varphi). \quad (12)$$

The expression for $R_y^\varphi \stackrel{\text{def}}{=} |\mathbf{y} - \mathbf{x}(\varphi)|$ is obtained similarly.

Define the total image as the sum of single-pulse images (5):

$$I(t_y, \mathbf{y}) = \sum_{n=-N/2}^{N/2} \int \overline{P\left(t - \frac{2R_y^n}{c} - t_y\right)} u_{\mathbf{x}^n}^s(t) dt = \sum_{n=-N/2}^{N/2} I_{\mathbf{x}^n}(t_y, \mathbf{y}), \quad (13)$$

where N is the total number of the pulse transmit-receive locations and \mathbf{x}^n are given by (10) for $\varphi = \varphi_n = n\varphi_T/N$. When $\{\varphi_n\}$ are sufficiently dense (see [12, section 2.4.2] or [10, section 4.5.3] for detail), the sum in (13) can be replaced with an integral over φ . Then, using (6), we obtain:

$$I(t_y, \mathbf{y}) \approx \frac{N}{\varphi_T} \int_{-\varphi_T/2}^{\varphi_T/2} I_{\mathbf{x}(\varphi)}(t_y, \mathbf{y}) d\varphi = \int_0^\infty dt_z \int d\mathbf{z} \nu(t_z, \mathbf{z}) W(t_y, \mathbf{y}; t_z, \mathbf{z}), \quad (14)$$

where

$$W(t_y, \mathbf{y}; t_z, \mathbf{z}) = \frac{N}{\varphi_T} \int_{-\varphi_T/2}^{\varphi_T/2} d\varphi \int dt P\left(t - \frac{2R_y^\varphi}{c} - t_y\right) P\left(t - \frac{2R_z^\varphi}{c} - t_z\right). \quad (15)$$

The most common SAR signal is a chirp:

$$P(t) = A(t) \exp(-i\omega_0 t), \quad \text{where} \quad A(t) = \chi_\tau(t) \exp(-i\alpha t^2) \quad (16)$$

and χ_τ is the indicator function:

$$\chi_\tau(t) = \begin{cases} 1, & t \in [-\tau/2, \tau/2], \\ 0, & \text{otherwise.} \end{cases} \quad (17)$$

Hereafter, we assume $\alpha > 0$ ('upchirp') so that the bandwidth $B = 2\alpha\tau$ is positive; the case $\alpha < 0$ can be treated similarly. We also assume a narrowband signal with a high time-bandwidth product: $B \ll \omega_0$ and $B\tau \gg 1$, which is also common for SAR. Using (12) and (16)–(17), we transform (15) into

$$W(t_y, \mathbf{y}; t_z, \mathbf{z}) = \frac{N}{\varphi_T} \int_{-\varphi_T/2}^{\varphi_T/2} d\varphi \exp(-2i\omega_0 T^\varphi) \int_{-\tau/2}^{\tau/2} d\tilde{t} \exp(-4i\alpha T^\varphi \tilde{t}), \quad (18)$$

where

$$\begin{aligned} T^\varphi &= \frac{R_y^\varphi - R_z^\varphi}{c} + \frac{t_y - t_z}{2} \\ &= \left(\frac{y_2 - z_2}{c} \cos \varphi - \frac{y_1 - z_1}{c} \sin \varphi \right) \sin \theta + \frac{t_y - t_z}{2}, \\ \tilde{t} &= t - \frac{R_y^\varphi - R_z^\varphi}{c} - \frac{t_y - t_z}{2}. \end{aligned} \quad (19)$$

In (18), we made a common simplification by disregarding the dependence of the integration limits on \mathbf{y} and \mathbf{z} for signals with $B\tau \gg 1$, see [12, chapter 2].

Note that T^φ is a function of $t_y, \mathbf{y}, t_z, \mathbf{z}$, and φ , while W is defined via an integral that involves T^φ . In particular, the interior integral in (18) can be evaluated as follows:

$$\begin{aligned} W_R &\equiv W_R(t_y, \mathbf{y}; t_z, \mathbf{z}; \varphi) \\ &= \int_{-\tau/2}^{\tau/2} d\tilde{t} \exp(-4i\alpha T^\varphi \tilde{t}) = \tau \operatorname{sinc}(BT^\varphi), \end{aligned}$$

where $\operatorname{sinc} \xi \stackrel{\text{def}}{=} \sin \xi / \xi$. Thus,

$$W(t_y, \mathbf{y}; t_z, \mathbf{z}) = \frac{N}{\varphi_T} \int_{-\varphi_T/2}^{\varphi_T/2} \exp(-2i\omega_0 T^\varphi) W_R(t_y, \mathbf{y}; t_z, \mathbf{z}; \varphi) d\varphi. \quad (20)$$

For T^φ given by (19), we will take the Taylor expansion of the trigonometric functions of φ about zero and explore the effect of its first three terms on expression (20). If we retain the zeroth-order term only, i.e. $\cos \varphi \approx 1$, $\sin \varphi \approx 0$, then the imaging kernel (18) does not depend on the cross-range coordinates y_1 and z_1 at all. Then, the radar will not be able to reconstruct any variation of ν in the cross-range direction, i.e. will provide no azimuthal resolution.

Expanding T^φ up to the linear term, i.e. $\cos \varphi \approx 1$, $\sin \varphi \approx \varphi$, we obtain:

$$\begin{aligned} W_{\text{lin}}(t_y, \mathbf{y}; t_z, \mathbf{z}) &= \exp(-2i\omega_0 T^0) \frac{N}{\varphi_T} \int_{-\varphi_T/2}^{\varphi_T/2} \exp(2ik_{0\theta}(y_1 - z_1)\varphi) W_R d\varphi \\ &= \tau \exp(-2i\omega_0 T^0) \frac{N}{\varphi_T} \int_{-\varphi_T/2}^{\varphi_T/2} \exp(2ik_{0\theta}(y_1 - z_1)\varphi) \\ &\quad \cdot \text{sinc}(BT_{\text{lin}}^\varphi) d\varphi, \end{aligned} \quad (21)$$

where

$$\begin{aligned} T^0 &= T^\varphi \Big|_{\varphi=0} = \frac{y_2 - z_2}{c} \sin \theta + \frac{t_y - t_z}{2}, \\ T_{\text{lin}}^\varphi &= T^0 - \sin \theta \frac{y_1 - z_1}{c} \varphi, \quad k_{0\theta} = \frac{\omega_0}{c} \sin \theta. \end{aligned} \quad (22)$$

Unlike previously, the imaging kernel W_{lin} of (21) does depend on the cross-range coordinates. Moreover, the range coordinates y_2 and z_2 appear only in combination with $(t_y - t_z)$ as in T^0 , see (22). This, in particular, means:

$$\begin{aligned} W_{\text{lin}}(t_y, \mathbf{y}; t_z, \mathbf{z}) &= W_{\text{lin}}\left(0, \mathbf{y} + \frac{ct_y}{2 \sin \theta} \mathbf{e}_2; t_z, \mathbf{z}\right) \\ &= W_{\text{lin}}\left(t_y, \mathbf{y}; 0, \mathbf{z} + \frac{ct_z}{2 \sin \theta} \mathbf{e}_2\right), \end{aligned} \quad (23)$$

and, due to (14),

$$I_{\text{lin}}(t_y, \mathbf{y}) = I_{\text{lin}}\left(0, \mathbf{y} + \frac{ct_y}{2 \sin \theta} \mathbf{e}_2\right), \quad (24)$$

where \mathbf{e}_2 is a unit vector in the range direction (see formula (8)). We see that the range-delay ambiguity is not resolved if we retain only the linear term with respect to φ in the expansion of T^φ (in this regard, expressions (23) and (24) are similar to their single-pulse counterparts (7) and (8), respectively).

Replacing T_{lin}^φ with T^0 under the sinc in (21) (but not in the exponent in (20), where the factor in front of φ is $2\omega_0/B \gg 1$ times bigger) allows us to integrate over φ and obtain the factorized expression¹:

$$W_{\text{lin}}(t_y, \mathbf{y}; t_z, \mathbf{z}) \approx \exp(-2i\omega_0 T^0) \cdot \underbrace{N \text{sinc}(k_{0\theta} \varphi_T (y_1 - z_1))}_{W_A} \cdot \underbrace{\tau \text{sinc}(BT^0)}_{W_R^0}, \quad (25)$$

where W_A and W_R^0 are the azimuthal and range factors of the imaging kernel, respectively. The case of a standard SAR (see also (9)) corresponds to ν given by (2) and $t_y = 0$, which turns formulae (14) and (25) into the following:

$$I_{\text{std}}(\mathbf{y}) \stackrel{\text{def}}{=} I_{\text{lin}}(0, \mathbf{y}) = \int d\mathbf{z} \nu_{\text{inst}}(\mathbf{z}) W_{\text{lin}}(0, \mathbf{y}; 0, \mathbf{x}) \stackrel{\text{def}}{=} \int d\mathbf{z} \nu_{\text{inst}}(\mathbf{z}) W_{\text{std}}(\mathbf{y}, \mathbf{z}), \quad (26)$$

¹ It has been shown in [12, chapter 2] and [25] that if we retain the dependence of W_R on φ (i.e. if we do not replace T^φ with T^0 under the sinc in (21), which is equivalent to replacing W_R with W_R^0 in (20)), then the difference between the expressions (20) and (25) is small, on the order of $N\tau B/\omega_0$ by absolute value, or about B/ω_0 in relative terms (this difference is called the factorization error).

where

$$W_{\text{std}}(\mathbf{y}, \mathbf{z}) = N\tau \exp(-2i\omega_0 \sin \theta (y_2 - z_2)/c) \cdot \text{sinc}(k_{0\theta} \varphi_T (y_1 - z_1)) \text{sinc}\left(B \frac{y_2 - z_2}{c} \sin \theta\right) \quad (27)$$

is the corresponding point spread function, and the three factors on the right hand side of (27) (excluding the factor $N\tau$) define the fast phase, cross-range response, and range response, respectively. The function $W_{\text{std}}(\mathbf{y}, \mathbf{z}_d)$ is proportional to the image of an instantaneous point scatterer:

$$\nu_{\text{inst}}(\mathbf{z}) = A\delta(\mathbf{z} - \mathbf{z}_d) \quad \text{where} \quad \mathbf{z}_d = (z_{d1}, z_{d2}, 0), \quad (28)$$

and hence the resolution in azimuth Δ_A and resolution in range Δ_R can be defined as semi-width of the main lobe of the corresponding sinc term. This yields:

$$|W_{\text{std}}(\mathbf{y}, \mathbf{z})| \sim \left| \text{sinc}\left(\pi \frac{y_1 - z_1}{\Delta_A}\right) \text{sinc}\left(\pi \frac{y_2 - z_2}{\Delta_R}\right) \right|,$$

where

$$\Delta_A = \pi \frac{1}{k_{0\theta} \varphi_T} \quad \text{and} \quad \Delta_R = \pi \frac{c}{B \sin \theta}. \quad (29)$$

The simplified expression (25) allows us to attribute the range-delay ambiguity to W_R^0 , which becomes the range factor of the imaging kernel in the case of a standard SAR, see (27). As the linearized approximation of T^φ given by (22) is found insufficient to resolve the range-delay ambiguity, we bring along the quadratic terms in the expansion of $\cos \varphi$ and $\sin \varphi$, which yields:

$$\cos \varphi \approx 1 - \frac{\varphi^2}{2}, \quad \sin \varphi \approx \varphi. \quad (30)$$

Using the same factorized approximation as in (25), we obtain:

$$W(t_y, \mathbf{y}; t_z, \mathbf{z}) \approx \exp(-2i\omega_0 T^0) W_R^0 \frac{N}{\varphi_T} \cdot \int_{-\varphi_T/2}^{\varphi_T/2} \exp(2ik_{0\theta}(y_1 - z_1)\varphi) \exp(ik_{0\theta}(y_2 - z_2)\varphi^2) d\varphi. \quad (31)$$

Similarly to [26, formula (59)], we introduce a function of two variables:

$$\Phi(v_1, v_2) \stackrel{\text{def}}{=} \int_{-1/2}^{1/2} \exp(2iv_1 s) \exp(iv_2 s^2) ds. \quad (32)$$

It is easy to show that

$$\Phi(v_1, 0) = \text{sinc } v_1 \quad \text{and} \quad \Phi(0, v_2) = \frac{C(t) + i \text{sign}(v_2)S(t)}{t}, \quad (33)$$

where $t = |v_2|^{1/2}(2\pi)^{-1/2}$ and $C(t)$ and $S(t)$ are the Fresnel integrals [27]. The absolute value of Φ , as well as the marginal functions (33), are plotted in figure 2. Both marginal functions have their peaks when the corresponding argument is zero. In doing so, the main lobe of $\Phi(v_1, 0)$ is clearly delineated by the zeros at $|v_1| = \pi$, yet the minima of $|\Phi(0, v_2)|$ at $|v_2| = b_\Phi \approx 23$ appear quite ‘shallow’. For $|v_2| \gtrsim 1$, the stationary phase analysis yields

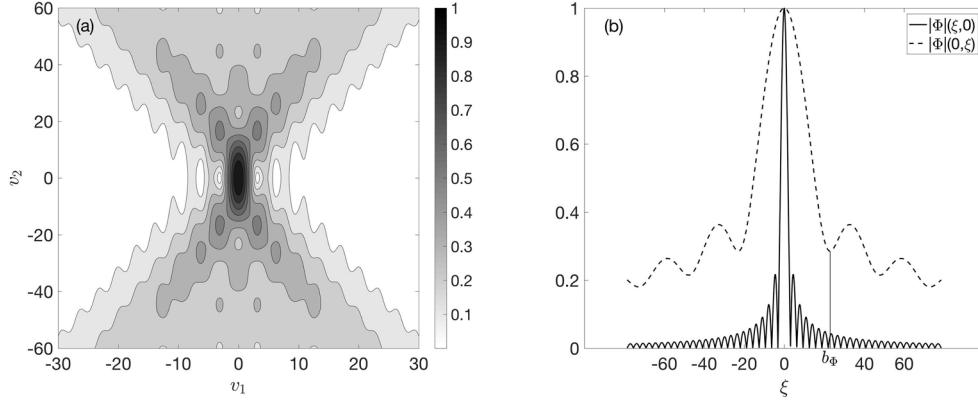


Figure 2. Left: Contour plot of $|\Phi|(v_1, v_2)$; Right: marginal functions (33) of $|\Phi|(v_1, v_2)$. The half-width of the main lobe of $|\Phi|(\xi, 0)$ is π , whereas that of $|\Phi|(0, \xi)$ is $b_\Phi \approx 23$.

$$|v_1| \leq |v_2|/2 \quad (34)$$

as the condition for the stationary point of the integral in (32) to be within the integration limits. When condition (34) is not satisfied, the value of the integral is small, as indicated by the white areas in the left panel of figure 2.

With the help of (32), formula (31) can be expressed as

$$W(t_y, \mathbf{y}; t_z, \mathbf{z}) = \exp(-2i\omega_0 T^0) \cdot N\Phi(k_{0\theta}\varphi_T(y_1 - z_1), k_{0\theta}\varphi_T^2(y_2 - z_2)) \cdot W_R^0, \quad (35)$$

where $W_R^0 = \tau \operatorname{sinc}(BT^0)$ as in (25), with T^0 defined by (22). This form of the imaging kernel will be used throughout the rest of this paper.

2.3. Properties of the coordinate-delay imaging operator

We are interested in how well the range-delay ambiguity described in section 2.1 is resolved when imaging with the help of the kernel (35). Formally, W is a function of six scalar arguments, although the particular form (35) indicates that we can reduce its set of arguments to only three independent variables: $(y_1 - z_1)$, $(y_2 - z_2)$, and $(t_y - t_z)$. This should be expected because, given some constant t_d and \mathbf{z}_d , the function $W(t_y, \mathbf{y}; t_d, \mathbf{z}_d)$ is proportional to the image due to a ‘space-time point scatterer’:

$$\nu(t_z, \mathbf{z}) = A\delta(t_z - t_d)\delta(\mathbf{z} - \mathbf{z}_d), \quad (36)$$

see (14), (26) and (28). The maximum of this image amplitude, or, equivalently, the maximum of $|W|$, is achieved at the space-time ‘location’ of the scatterer (36), i.e. when $(y_1 - z_1) = 0$, $(y_2 - z_2) = 0$, and $(t_y - t_z) = 0$. The range-delay ambiguity will be caused by a slow decay of $|W|$ along certain directions in the space of its arguments.

Similarly to (7), the range coordinates are tied with the delay in W_R^0 :

$$\begin{aligned} W_R^0 &= \tau \operatorname{sinc}(BT^0) = \tau \operatorname{sinc}\left[B\left(\frac{y_2 - z_2}{c} \sin \theta + \frac{t_y - t_z}{2}\right)\right] \\ &= \tau \operatorname{sinc}\left[\pi \frac{1}{\Delta_R} \left(y_2 - z_2 + c \frac{t_y - t_z}{2 \sin \theta}\right)\right]. \end{aligned} \quad (37)$$

However, the range coordinate $(y_2 - z_2)$ stands separate from the delays in the second argument of Φ , see (35). Hence, it is possible to use the semi-width of the main lobe of the dashed curve in the right panel of figure 2 to define the ‘unambiguous’ resolution size due to the second argument of Φ :

$$\Delta_U = \frac{b_\Phi}{k_{0\theta}\varphi_T^2}. \quad (38)$$

It is therefore the interaction of the two factors in (35), W_R^0 and Φ , that will determine how the range-delay ambiguity manifests itself. Both factors depend on the range coordinates and both decay as $|y_2 - z_2| \rightarrow \infty$:

$$|W_R^0| \sim \left| \pi \frac{y_2 - z_2}{\Delta_R} \right|^{-1}, \quad |\Phi| \sim \left| \frac{b_\Phi}{\pi} \frac{y_2 - z_2}{\Delta_U} \right|^{-1/2}. \quad (39)$$

The first estimate (39) holds assuming that $(t_y - t_z)$ is fixed in the argument of W_R^0 , see (37). The second estimate (39) can be obtained by applying the stationary phase formula to (32) provided (34) is satisfied.

We introduce the following parameter to describe the ratio between the two scales in (39):

$$\kappa \stackrel{\text{def}}{=} \varphi_T^2 \frac{\omega_0}{B}. \quad (40)$$

When $\Delta_R \ll \Delta_U$ (or, equivalently, $\kappa \ll b_\Phi/\pi \approx 7$), the main lobe of W in the range direction (i.e. as a function of $(y_2 - z_2)$ with $y_1 = z_1$ and $t_y = t_z$) is determined by W_R^0 because the factor Φ in (35) for $B|y_2 - z_2| \sin \theta/c \lesssim \pi$ can approximately be replaced with one. In the opposite case of $\Delta_R \gg \Delta_U$, or $\kappa \gg b_\Phi/\pi$, the main lobe of W in the range direction for $B|y_2 - z_2| \sin \theta/c \lesssim \pi$ is determined by the function Φ of (32). We will call $\kappa \ll b_\Phi/\pi$ and $\kappa \gg b_\Phi/\pi$ the narrow-aperture and wide-aperture modes, respectively.

For a narrow-aperture regime, the resolution of the system in range is due to W_R^0 . In this case, $\Phi(\dots)$ in (35) turns into $\text{sinc}(k_{0\theta}\varphi_T(y_1 - z_1))$ as $\kappa \rightarrow 0$, so (35) reduces to (25). However, the factor W_R^0 is subject to the range-delay ambiguity, while the range resolution due to $\Phi(\dots)$ is much larger:

$$|y_2 - z_2| \gtrsim \frac{b_\Phi}{k_{0\theta}\varphi_T^2} = \Delta_R \frac{b_\Phi}{\pi\kappa} \gg \Delta_R. \quad (41)$$

The geometry of the narrow-aperture images can be understood as follows. As the antenna is far away, see (12), we define the ambiguity directions:

$$\text{‘ambiguity direction in } \mathbf{z}\text{’} \stackrel{\text{def}}{=} \left(t_z + \frac{2z_2 \sin \theta}{c} = \text{const}, z_1 = \text{const} \right), \quad (42a)$$

$$\text{‘ambiguity direction in } \mathbf{y}\text{’} \stackrel{\text{def}}{=} \left(t_y + \frac{2y_2 \sin \theta}{c} = \text{const}, y_1 = \text{const} \right). \quad (42b)$$

The right-hand side of (42a) specifies a direction in the ‘coordinates’ $(z_1, z_2, \frac{ct_z}{2 \sin \theta})$ as the intersection of a plane from the family $t_z + \frac{2z_2 \sin \theta}{c} = \text{const}$ with a plane from the family $z_1 = \text{const}$, while (42b) does the same for $(y_1, y_2, \frac{ct_y}{2 \sin \theta})$. A straight line given by such an intersection will be called an ambiguity line. The analysis in sections 2.1 and 2.2 shows that the images due to the kernel W_{lin} of (25) are insensitive to the variations of $\nu(t_z, \mathbf{z})$ that preserve the integral of ν along the ambiguity direction in \mathbf{z} , see (42a), (23), and (4); at the same time, such images are constant along the ambiguity direction in \mathbf{y} , see (42b) and (24).

The effect of the quadratic term in (30) is controlled by the parameter κ of (40). For example, inequality (41) means that the image of a point scatterer (36) will be stretched along the ambiguity line passing through the ‘point’ $(y_1, y_2, \frac{ct_y}{2\sin\theta}) = (z_{d1}, z_{d2}, \frac{ct_d}{2\sin\theta})$. At the same time, the characteristics of this image in the plane $t_y = 0$ are still defined by (29), which means that, unlike in sub-banding [3], no formal concession in range resolution is made in the attempt to achieve resolution in the delay variable (see also [6]).

For the wide-aperture case (large κ), the range resolution is formally due to Φ and there is no ambiguity. However, high sidelobes and slow decay of $|\Phi|$ in its second argument, as per the second equation (39) and the right panel of figure 2, make it difficult to achieve the range resolution comparable to Δ_U of (38), see also [6, 19, 21]. Hence, in practice the resolution in range is still given by Δ_R of (29). This may negatively impact the imaging in azimuth as well. Indeed, using (35) we can write:

$$|W| \propto \left| \Phi(v_1, v_2) \cdot W_R^0\left(\frac{v_2}{\kappa}\right) \right|,$$

where $v_1 = k_{0\theta}\varphi_T(y_1 - z_1)$ and $v_2 = k_{0\theta}\varphi_T^2(y_2 - z_2)$. Then, taking $|y_2 - z_2| \sim \Delta_R$ in (34), we see that for large κ the corresponding azimuthal width of $\Phi(\dots)$ shown in the left panel of figure 2 becomes:

$$|y_1 - z_1| \sim \frac{1}{2}\varphi_T\Delta_R = \frac{1}{2}\Delta_A\kappa \gg \Delta_A. \quad (43)$$

To highlight the role of the ambiguity directions introduced in (42), we change the coordinates:

$$\begin{aligned} \eta &= k_{0\theta}\varphi_T(y_1 - z_1), \\ \zeta &= \frac{B}{\omega_0}k_{0\theta}\left(y_2 - z_2 + \frac{1}{\sin\theta}\frac{c(t_y - t_z)}{2}\right), \\ \psi &= \frac{B}{\omega_0}k_{0\theta}\left(y_2 - z_2 - \frac{1}{\sin\theta}\frac{c(t_y - t_z)}{2}\right). \end{aligned} \quad (44)$$

In (44), ζ and ψ are the coordinates across and along the ambiguity lines, respectively. Then, expression (35) takes the following form:

$$W(\eta, \zeta, \psi) = N\tau \exp\left(-2i\frac{\omega_0}{B}\zeta\right) \cdot \Phi\left(\eta, \kappa\frac{\zeta + \psi}{2}\right) \cdot \text{sinc } \zeta. \quad (45)$$

The central peak of W is well defined along η and ζ coordinates. However, if we fix η and ζ , then there is only a slow decay, $\sim \psi^{-1/2}$, in the ambiguity directions in (42), see the second estimate of (39).

When an ambiguity line with $\eta = 0$ intersects the planes $t_y = 0$ and $y_2 = z_{d2}$ (or, in the target coordinates, $t_z = 0$ and $z_2 = z_{d2}$, respectively, with $z_1 = z_{d1}$ in both cases), the resulting pair of coordinate-delay ‘points’ will be called an ambiguity pair, see figure 3. This concept will be helpful in illustrating how delayed scatterers produce range streaks in SAR images (figure 4 provides an example). Consider a point scatterer at $\mathbf{z} = \mathbf{z}_d$ that exhibits delayed scattering for $0 \leq t_z \leq t_{\max}$. On a standard SAR image $I(0, \mathbf{y})$, it will show up as a streak in the range direction. This streak can be understood as the intersection of the family of ambiguity lines drawn through the support of $\nu(t_z, \mathbf{z})$, i.e.

$$y_1 = z_{d1}, \quad y_2 = z_{d2} - \frac{c}{\sin\theta}\frac{t_y - t_z}{2}, \quad 0 \leq t_z \leq t_{\max},$$

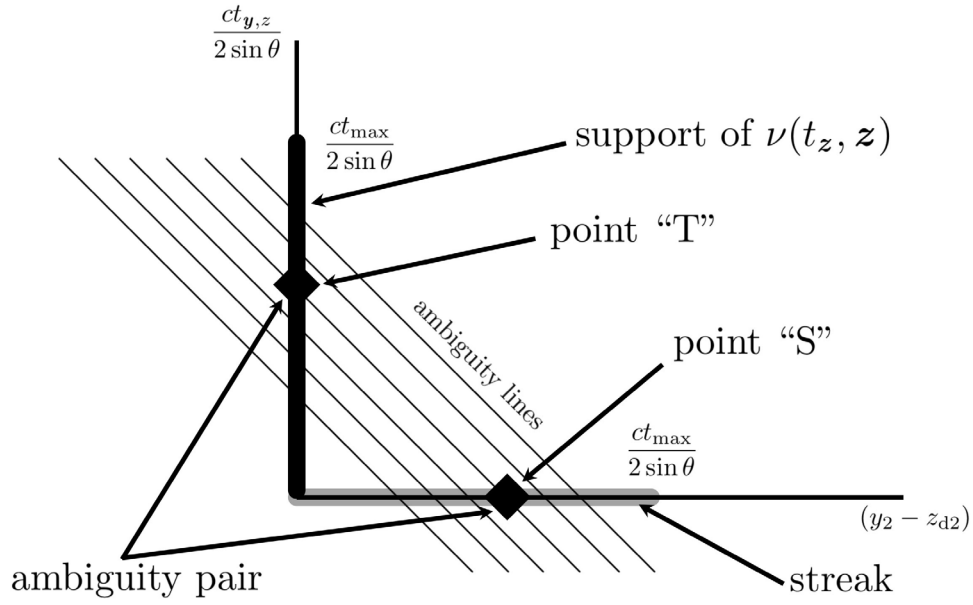


Figure 3. Ambiguity lines (42), ambiguity pair, and the streak due to a delayed scatterer.

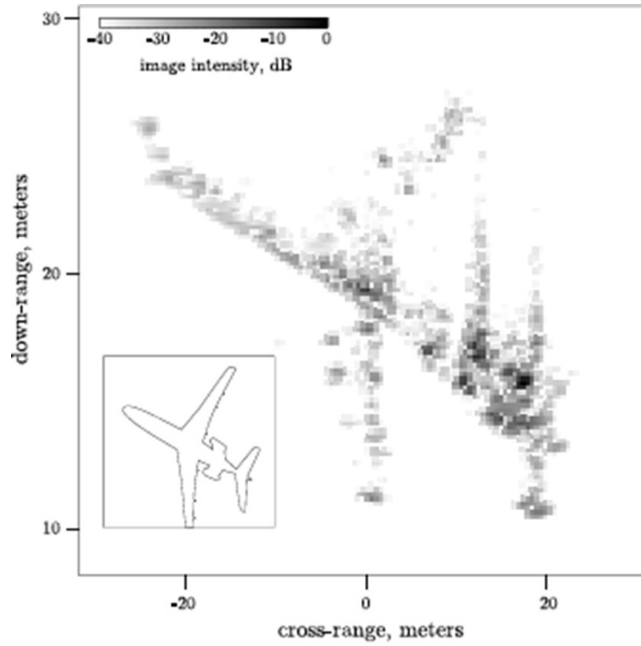


Figure 4. This image of an aircraft shows streaks due to engine inlets [13].

with the plane $t_y = 0$. If $t_{\max} \gg B^{-1}$, then the streak extends to the distance of $ct_{\max}/(2 \sin \theta) \gg \Delta_R$ behind the true location of the scatterer $y_2 = z_{d2}$. On a standard SAR image, it can incorrectly be interpreted as a linear instantaneous scatterer between z_d and $z_d + (ct_{\max}/(2 \sin \theta))\mathbf{e}_2$, see figure 3.

On the other hand, the coordinate-delay SAR provide two values of $|I|$ for each ambiguity pair (the image I is defined by (14)). The difference between these values is due to the argument ψ in (45). Taking, for definiteness, $t_z = t_{\max}$ and using (38)–(39), we can observe that if

$$\frac{ct_{\max}}{2 \sin \theta} \gg \Delta_U, \quad \text{or, equivalently,} \quad \frac{\kappa B t_{\max}}{2} \gg b_\Phi, \quad (46)$$

then for a delayed scatterer, the value of $|I|$ taken within the support of $\nu(t_z, \mathbf{z})$ (i.e. at the point ‘T’ in figure 3) will be larger than that taken in the streak (point ‘S’). For an instantaneous scatterer, it will be the other way around. Hence, if condition (46) is satisfied, it appears feasible to discriminate between these two targets by analyzing the ambiguity pairs in the coordinate-delay SAR images. Note that for $t_{\max} \gg 1/B$, this can be realized even in a narrow-aperture case, see (40).

To be practical though, the foregoing approach to the detection of delayed returns (see also [6]) should be able to deal with extended targets. Scattering off extended targets involves resonant mechanisms that are not captured by merely considering, say, $\nu_{\text{inst}}(\mathbf{z})$ in (26) with extended support (see [18] and [12, chapter 7]). Moreover, extended scatterers exhibit speckle [7, 9], a very significant phenomenon in SAR imaging that cannot be simulated by deterministic functions $\nu(t_z, \mathbf{z})$ or $\nu_{\text{inst}}(\mathbf{z})$. In realistic setups, the effect of speckle combined with high sidelobes of Φ has to be addressed. This will be the subject of subsequent sections.

3. Speckle in SAR targets

3.1. Speckle in homogeneous scatterers

The scattering properties of radar targets are characterized by multi-scale behavior. On the scale comparable to the wavelength $\lambda = 2\pi c/\omega_0$, the reflectivity is rough. It is this small-scale roughness that gives rise to the Bragg resonant mechanism of surface scattering and, in particular, enables the backscattering, which is critical for SAR, see [18] and [12, chapter 7].

At the same time, the quantities of interest in remote sensing are typically some averaged parameters that characterize the target. They are expected to vary gradually on the scale comparable to the resolution size $\Delta_{R,A} \gg \lambda$. In practice, however, this does not happen. The coherent mechanism of SAR imaging leads to the phenomenon of speckle. Speckle makes the image inherit some of the small-scale roughness and thus look ‘bumpy’ even on the scale where the parameters of interest are smooth. Speckle is considered a nuisance because it significantly affects our ability to resolve small-scale or low-contrast variations of average reflectivity of the scene. A detailed description of the effect of speckle can be found in [8, 9], and [28, chapter 18].

The standard SAR theory for instantaneous targets is built upon the model of a point target: $\nu_{\text{inst}}(\mathbf{z}) = A\delta(\mathbf{z} - \mathbf{z}_d)$, see (28), where the scatterer location \mathbf{z}_d and amplitude A are constants. Despite dominating the SAR literature, neither does this model describe speckle nor can it be easily modified to the case of extended scatterers, i.e. scatterers with non-singular support, see [9] and [12, chapter 7]. The approach described in section 2, see also [6], is an extension of the standard SAR to images that depend on one additional ‘coordinate’, namely, t_y , see (36). As for the speckle, however, it can be described efficiently only in the stochastic framework.

Next, we are going to build a model for a scatterer with non-singular support in time and/or space. It will rely on the treatment of extended (sometimes also called distributed) targets as presented in [9]. In particular, the homogeneous instantaneous reflectivity, or background, is modeled by a random function $\nu_b(t_z, \mathbf{z})$ that has the following form (see (2)):

$$\nu_b(t_z, \mathbf{z}) = \delta(t_z) \mu_b(\mathbf{z}). \quad (47)$$

In (47), $\mu_b(\mathbf{z})$ is a circular Gaussian white random field with the variance σ_b^2 (see [29–31]):

$$\mu_b(\mathbf{z}) = \text{Re } \mu_b(\mathbf{z}) + i \text{Im } \mu_b(\mathbf{z}), \quad (48)$$

where $\text{Re } \mu_b(\mathbf{z})$ and $\text{Im } \mu_b(\mathbf{z})$ are independent real-valued zero-mean white Gaussian noise fields with the intensity $\frac{\sigma_b^2}{2}$:

$$\begin{aligned} \langle \text{Re } \mu_b(\mathbf{z}) \rangle &= 0, & \langle \text{Re } \mu_b(\mathbf{z}) \text{Re } \mu_b(\mathbf{z}') \rangle &= \frac{\sigma_b^2}{2} \delta(\mathbf{z} - \mathbf{z}'), \\ \langle \text{Im } \mu_b(\mathbf{z}) \rangle &= 0, & \langle \text{Im } \mu_b(\mathbf{z}) \text{Im } \mu_b(\mathbf{z}') \rangle &= \frac{\sigma_b^2}{2} \delta(\mathbf{z} - \mathbf{z}'), \end{aligned} \quad (49)$$

so that

$$\langle \mu_b(\mathbf{z}) \rangle = 0, \quad \langle \mu_b(\mathbf{z}) \mu_b(\mathbf{z}') \rangle = 0, \quad \langle \overline{\mu_b(\mathbf{z})} \mu_b(\mathbf{z}') \rangle = \sigma_b^2 \delta(\mathbf{z} - \mathbf{z}'). \quad (50)$$

In (49) and (50), $\delta(\mathbf{z}) \equiv \delta(z_1) \delta(z_2)$ according to (11), $\langle \dots \rangle$ denotes statistical averaging, and σ_b^2 is a deterministic positive constant that characterizes the statistically averaged reflectivity of the background.

There is more than one way of defining delta-correlated processes, including their non-stationary and multi-dimensional versions, see [29, 32–37]. The notion of a Gaussian white noise as introduced in (49) requires additional clarification. It is a delta-correlated stochastic process with continuous argument. It is known, however, that random variables with infinite variances cannot be Gaussian. So the word ‘Gaussian’ as applied to the delta-correlated process μ_b of (48)–(50) means that it is required to generate a conventional Gaussian process by convolution with the imaging kernel, see (14). Moreover, for σ_b^2 independent of \mathbf{z} , we will call the processes (49) and (50) stationary. In a more realistic treatment that is not attempted in this study, σ_b^2 can vary with \mathbf{z} on the scale $\gtrsim \Delta_{A,R}$, see the discussion in the beginning of this section.

The use of a random reflectivity function, such as ν_b of (47)–(50), in the imaging operator (14) makes the resulting image $I_b(t_y, \mathbf{y})$ a random function as well. The presence of the delta function in (47) eliminates integration over t_z in (14). Then, the first two formulas in (50) immediately yield

$$\langle I_b(t_y, \mathbf{y}) \rangle = 0, \quad \langle I_b(t_y, \mathbf{y}) I_b(t'_y, \mathbf{y}') \rangle = 0. \quad (51a)$$

Multiplying (14) by its conjugate, taking the average of the result, and using the delta function in (50) along with the explicit form of W in (35), we obtain:

$$\langle |I_b(t_y, \mathbf{y})|^2 \rangle = N^2 \tau^2 \sigma_b^2 \int \text{sinc}^2(\zeta_0) |\Phi(k_{0\theta} \varphi_T(y_1 - z_1), k_{0\theta} \varphi_T^2(y_2 - z_2))|^2 d\mathbf{z}, \quad (51b)$$

$$\begin{aligned} \langle \overline{I_b(t_y, \mathbf{y})} I_b(t'_y, \mathbf{y}') \rangle &= N^2 \tau^2 \sigma_b^2 \exp(2ik_{0\theta}(y_2 - y'_2)) \exp(i\omega_0(t_y - t'_y)) \\ &\quad \cdot \int \text{sinc}(\zeta_0) \overline{\Phi(k_{0\theta} \varphi_T(y_1 - z_1), k_{0\theta} \varphi_T^2(y_2 - z_2))} \\ &\quad \cdot \text{sinc}(\zeta'_0) \Phi(k_{0\theta} \varphi_T(y'_1 - z_1), k_{0\theta} \varphi_T^2(y'_2 - z_2)) d\mathbf{z}, \end{aligned} \quad (51c)$$

where $d\mathbf{z} = dz_1 dz_2$, see (11), and

$$\zeta_0 = BT^0 \Big|_{t_z=0} = \frac{B}{\omega_0} k_{0\theta} (y_2 - z_2) + \frac{Bt_y}{2}, \quad \zeta'_0 = \frac{B}{\omega_0} k_{0\theta} (y'_2 - z_2) + \frac{Bt'_y}{2}.$$

As expected for a homogeneous scatterer (50), expression (51b) does not depend on \mathbf{y} because the integrand on the right-hand side of (51b) depends on the integration variable \mathbf{z} only via $(\mathbf{y} - \mathbf{z})$, and the integration is performed over the entire space. We can see that the values of I become decorrelated:

$$|\langle \overline{I_b(t_y, \mathbf{y})} I_b(t'_y, \mathbf{y}') \rangle|^2 \ll \langle |I_b(t_y, \mathbf{y})|^2 \rangle \langle |I_b(t'_y, \mathbf{y}')|^2 \rangle, \quad (52)$$

when the peaks of the functions in the integrand of (51c) significantly separate:

$$|\zeta_0 - \zeta'_0| \gtrsim \pi \quad \text{or} \quad |\eta - \eta'| \equiv k_{0\theta} \varphi_T |y_1 - y'_1| \gtrsim \max(\pi, \pi\kappa/2). \quad (53)$$

Note that the second inequality in (53) addresses both the first and second argument of Φ , see (43) and the discussion right before it. On the other hand, if we fix two coordinate-delay ‘points’, (t_y, \mathbf{y}) and (t'_y, \mathbf{y}') , on the same ambiguity line:

$$y_1 = y'_1, \quad \frac{B}{\omega_0} k_{0\theta} y_2 + \frac{Bt_y}{2} = \frac{B}{\omega_0} k_{0\theta} y'_2 + \frac{Bt'_y}{2}, \quad |t_y - t'_y| = \text{const},$$

e.g. take an ambiguity pair as shown in figure 3, then the inequality in (52) becomes an equality as $\kappa \rightarrow 0$. In other words, in the narrow-aperture case, the image values along the ambiguity lines are strongly correlated.

The Gaussianity of the random field $I_b(t_y, \mathbf{y})$ is corroborated by experimental evidence [8, 9, 38]. In our analysis, it is a requirement imposed on $\mu_b(\mathbf{z})$, see the discussion after (50). As a consequence, we have:

$$\text{Var}(|I_b(t_y, \mathbf{y})|^2) = \langle |I_b(t_y, \mathbf{y})|^4 \rangle - \langle |I_b(t_y, \mathbf{y})|^2 \rangle^2 = \langle |I_b(t_y, \mathbf{y})|^2 \rangle^2. \quad (54)$$

It means, in particular, that when the image is a circular Gaussian random field, the difference between the intensity $|I_b|^2$ in the neighboring pixels may often be comparable to its average. It is this property of the random field $I_b(0, \mathbf{y})$ that is responsible for speckle [7–9]; it creates visual roughness and presents major difficulties in analyzing SAR images of extended scatterers.

The derivation of relations (47)–(50) from first principles, based on the shape and dielectric properties of the scatterer, may be complicated. The model (47)–(50) is still convenient, because when combined with the assumption of circular Gaussianity, it allows us to establish certain useful relations between the image moments, see (51) and (54). The latter, in turn, facilitate the efficient image processing.

3.2. Inhomogeneous image components

In SAR images, the streaks due to delayed scattering (see, e.g. [6, figure 1], [39], as well as figure 4)² appear rugged, similarly to the speckle that was considered in section 3.1. For this reason, we will introduce two extensions of the speckle-producing scatterer model (47)–(50). First, we will describe a scatterer localized in space and exhibiting a delta-correlated delayed return. Henceforth, this model will be called a ‘t-scatterer’:

²The examples where streaks can be clearly seen are usually found in Inverse SAR (ISAR) observations of aircraft where there is no background obscuring the streak. An example where a streak is visible on a SAR image of the Earth surface can be found in [6, figure 1].

$$\nu_t(t_z, \mathbf{z}) \equiv \nu_t(t_z, \mathbf{z}; \mathbf{z}_d) = \mu_t(t_z) \delta(\mathbf{z} - \mathbf{z}_d). \quad (55)$$

In (55), μ_t is a non-stationary circular Gaussian white noise (c.f. (48)–(50)):

$$\langle \mu_t(t) \rangle = 0, \quad \langle \mu_t(t) \mu_t(t') \rangle = 0, \quad \langle \overline{\mu_t(t)} \mu_t(t') \rangle = \sigma_t^2 F_t(Bt/2) \delta(t - t'), \quad (56)$$

where \mathbf{z}_d is the location of the scatterer. Similarly to (50), we will call σ_t^2 the reflectivity of the t-scatterer, whereas $F_t = F_t(\zeta)$ defines the dimensionless intensity of the return as a function of time. To make sure that the scattering model (56) is causal, we require that $F_t(Bt/2) = 0$ for $t < 0$, see (1). For $t > 0$, we assume that $F_t(Bt/2) \geq 0$. In [37], the existence of a process that satisfies (56) is shown when the function $F_t(\zeta)$ is integrable on $(-\infty, \infty)$. From the standpoint of physics, this also limits the total power reflected by a scatterer of this type. In this work, we will take F_t as an indicator function:

$$F_t(\zeta) = \begin{cases} 1, & 0 \leq \zeta \leq \zeta_{\max}, \\ 0, & \text{otherwise,} \end{cases} \quad (57)$$

where the value of ζ_{\max} will be discussed later (see section 4.1). Then, similarly to I_b , the image I_t , which is given by (14) applied to ν_t of (55), is circular Gaussian, and the properties (51a) and (54) hold for $I_t(t_y, \mathbf{y})$ as well.

In standard SAR images, a t-scatterer described by (55) and (56) may be confused with a linearly shaped inhomogeneity of the background intensity aligned with the range direction (see figure 3). The corresponding instantaneous scatterer will henceforth be called an ‘s-scatterer’:

$$\nu_s(t_z, \mathbf{z}) \equiv \nu_s(t_z, \mathbf{z}; \mathbf{z}_d) = \delta(t_z) \delta(z_1 - z_{d1}) \mu_s(z_2 - z_{d2}), \quad (58)$$

where

$$\langle \mu_s(s) \rangle = 0, \quad \langle \mu_s(s) \mu_s(s') \rangle = 0, \quad \langle \overline{\mu_s(s)} \mu_s(s') \rangle = \sigma_s^2 F_s(Bk_{0\theta}s/\omega_0) \delta(s - s'). \quad (59)$$

Linearly-shaped inhomogeneities of instantaneous reflectivity, as in (58) and (59), may be representatives of roads, fences, edges of buildings, pipelines, etc. The three factors on the right hand side of the last equation in (59) are similar to those in (56). The process μ_s is a non-stationary circular Gaussian white noise. Causality imposes no restriction on F_s . However, similarly to ν_t of (55) and (56), we assume that $F_s(\zeta) = 0$ for $\zeta < 0$.

We have introduced the scatterer models (55) and (56) and (58) and (59) as an alternative to the space-time point scatterer (36) studied in [6]. In particular, the form (55) and (56) allows us to gather the signals reflected from the same target with different delays and analyze the resulting data. Similarly to the models developed in [1, chapter 4] and [13], we will only analyze the scenarios where the response delay of the scatterer ν_t of (55) and (56) does not exceed a certain predetermined maximum. However, the correlation properties of the scattered signal due to ν_t will differ from those considered in [1] or [13].

4. Discrimination between scatterer types in the presence of background and noise

4.1. Images due to inhomogeneous targets

Let us introduce the dimensionless coordinates for the image, see (44), with the origin at $(t_y, \mathbf{y}) = (0, \mathbf{z}_d)$:

$$(\eta_y, \zeta_y, \psi_y) = (\eta, \zeta, \psi) \Big|_{t_z=0, z=z_d}. \quad (60)$$

Similarly to (51), it is easy to obtain the expected values of image intensities for the scatterers described in section 3.2. The ambiguity lines in the coordinates (60) are $\{\eta_y = \text{const}, \zeta_y = \text{const}\}$. Substituting (55)–(59) into (14) and using (35), we have:

$$\begin{aligned} \langle |I_s|^2 \rangle (\eta_y, \zeta_y, \psi_y) &= N^2 \tau^2 \sigma_s^2 \frac{\omega_0}{Bk_{0\theta}} \\ &\quad \cdot \int_0^\infty F_s(\zeta') \text{sinc}^2(\zeta_y - \zeta') \left| \Phi \left[\eta_y, \kappa \left(\frac{\zeta_y + \psi_y}{2} - \zeta' \right) \right] \right|^2 d\zeta', \\ \langle |I_t|^2 \rangle (\eta_y, \zeta_y, \psi_y) &= N^2 \tau^2 \sigma_t^2 \frac{2}{B} \left| \Phi \left[\eta_y, \kappa \frac{\zeta_y + \psi_y}{2} \right] \right|^2 \\ &\quad \cdot \int_0^\infty F_t(\zeta') \text{sinc}^2(\zeta_y - \zeta') d\zeta'. \end{aligned} \quad (61)$$

Two different expressions (61) yield two different locations of the maximum image intensity (average) along the ambiguity line. Consider, for simplicity, the case of $\eta_y = 0$ and both $F_s(\zeta)$ and $F_t(\zeta)$ given by (57). Note that $\text{sinc}^2(\zeta_y - \zeta')$ has its central lobe on the interval $[-\pi, \pi]$ of its argument and decays quadratically for large arguments. Take $\zeta_{\max} \gg \pi$. Then, for ζ_y satisfying $\pi \ll \zeta_y \ll \zeta_{\max}$, see (57), the value of either integral in (61) will not change significantly if the integration limits are replaced with $(-\infty, \infty)$ and $F_t(\zeta')$ and $F_s(\zeta')$ are replaced with 1 for all arguments.

$$\begin{aligned} \langle |I_s|^2 \rangle (\eta_y, \zeta_y, \psi_y) &\approx N^2 \tau^2 \sigma_s^2 \frac{\omega_0}{Bk_{0\theta}} \\ &\quad \cdot \int_{-\infty}^\infty \text{sinc}^2(\zeta_y - \zeta') \left| \Phi \left[\eta_y, \kappa \left(\frac{\zeta_y + \psi_y}{2} - \zeta' \right) \right] \right|^2 d\zeta', \\ \langle |I_t|^2 \rangle (\eta_y, \zeta_y, \psi_y) &\approx N^2 \tau^2 \sigma_t^2 \frac{2}{B} \left| \Phi \left[\eta_y, \kappa \frac{\zeta_y + \psi_y}{2} \right] \right|^2 \\ &\quad \cdot \int_{-\infty}^\infty \text{sinc}^2(\zeta_y - \zeta') d\zeta'. \end{aligned} \quad (62)$$

Therefore, the maximum of $\langle |I_s|^2 \rangle$ as a function of ψ_y is achieved when the peaks of $\text{sinc}^2(\zeta_y - \zeta')$ and $|\Phi(0, \kappa(\dots - \zeta'))|^2$ as functions of ζ' overlap, i.e. for $\psi_y \approx \zeta_y$ ³. As for $\langle |I_t|^2 \rangle$ as a function of ψ_y , it reaches its maximum value when $|\Phi|^2$ peaks with respect to its second argument, i.e. at $\psi_y = -\zeta_y$. For a given ambiguity line, the locations of these maxima correspond to the points ‘S’ and ‘T’, respectively, of the ambiguity pair, see figure 3. Thus, one can see a similarity between the expectations (62) and images of a deterministic point target (36) considered in section 2.3.

The main lobe of $|\Phi(0, \cdot)|^2$ can be thought of as confined to the interval $[-b_\Phi, b_\Phi]$, see the right panel in figure 2. Then, we may argue that for a given ambiguity line the peaks of $\langle |I_s(0, \zeta_y, \cdot)|^2 \rangle$ and $\langle |I_t(0, \zeta_y, \cdot)|^2 \rangle$ are well separated if

$$\kappa \zeta_y \gtrsim b_\Phi,$$

³ Since functions $\text{sinc}^2(\cdot)$ and $|\Phi|^2(0, \cdot)$ are even and have local maxima at zero, it can be shown that ζ_y is a local maximum of $\langle |I_s|^2 \rangle(0, \zeta_y, \cdot)$ given by (61). We can also demonstrate numerically that it is a global maximum.

which is similar to condition (46) obtained for the deterministic case. It is also easy to see that the dependence of both expressions (62) on ψ_y becomes weaker and eventually vanishes as $\kappa \rightarrow 0$.

We have just shown that for a fixed $\kappa > 0$, the bigger the ζ_y , the better the separation between the peaks of $\langle |I_s(0, \zeta_y, \cdot)|^2 \rangle$ and $\langle |I_t(0, \zeta_y, \cdot)|^2 \rangle$. Hence, for a discrimination procedure outlined after (46), we should take the largest possible values of ζ_y . However, the functions F_s and F_t differ from zero only on a finite interval, see (57), and there are several considerations that lead to choosing a particular value of ζ_{\max} . On one hand, we may have an *a priori* knowledge about the maximum duration t_{\max} of the delayed response, so that

$$\zeta_y \leq \zeta_{\max} \leq \frac{Bt_{\max}}{2}. \quad (63a)$$

On the other hand, there may exist a maximum extent in range, s_{\max} , at which the background (50) can be considered homogeneous. Hence,

$$\zeta_y \leq \zeta_{\max} \leq \frac{Bk_{0\theta}s_{\max}}{\omega_0}. \quad (63b)$$

Hereafter, we will consider ζ_{\max} to be a parameter of the formulation that satisfies inequalities (63). Moreover, we must have $\kappa\zeta_{\max} \gtrsim b_\Phi$ in order to distinguish between the statistically averaged image intensities due to delayed and instantaneous targets as defined in section 3.2.

Recalling the definition of κ in (40), we can see that the inequality $\kappa\zeta_{\max} \gtrsim b_\Phi$ yields a condition that the angle φ_T should satisfy:

$$b_\Phi \lesssim \kappa\zeta_{\max} = \varphi_T^2 \cdot \min(\omega_0 t_{\max}/2, k_{0\theta}s_{\max}). \quad (64)$$

The following geometrical interpretation is therefore possible. In the target domain, the space-time point (t_{\max}, \mathbf{z}_d) is ambiguous with the ‘instantaneous’ point $(0, \mathbf{z}_d + s\mathbf{e}_2)$, where $s = ct_{\max}/(2 \sin \theta)$. The condition $\kappa\zeta_{\max} \gtrsim b_\Phi$ means that the two-way travel distance difference $2(|\mathbf{x} - \mathbf{z}_d| - |\mathbf{x} - (\mathbf{z}_d + s\mathbf{e}_2)|)$ varies by at least $(b_\Phi/2\pi)\lambda \approx 3\lambda$ as \mathbf{x} scans the synthetic aperture of angular width φ_T . An analogy can be found in the expression (29) for Δ_A : it corresponds to the angle φ_T such that for a pair of points \mathbf{z} and $(\mathbf{z} + \Delta_A \mathbf{e}_1)$, the similar variation of the two-way travel path difference $2cT_{\text{in}}^\varphi$ (see (22)) equals to λ .

4.2. Image sampling and the approach to discrimination in general

The effect of speckle on the detection of maxima of the quantities (62) will be similar to that of noise. A well-known strategy for detecting a weak signal in the presence of noise is to collect the signal over a sufficiently long time so that the effect of noise would average out and hence decrease due to its statistical properties. We will adjust this strategy to the case of delayed responses in SAR imaging. The ‘weak signal’ will be the variation of the average image intensity along the ambiguity lines, see figure 3 and the discussion around equations (61)–(62). As a counterpart to collecting the weak signal over a long interval, we will sample the image at multiple spatial locations and delays.

We assume that we have to distinguish between two possible configurations of scatterers in the target:

$$\nu(t_z, \mathbf{z}) = \nu_{s\text{-model}}(t_z, \mathbf{z}; \mathbf{z}_d) = \nu_b(t_z, \mathbf{z}) + \nu_s(t_z, \mathbf{z}; \mathbf{z}_d) \quad (65a)$$

and

$$\nu(t_z, \mathbf{z}) = \nu_{\text{t-model}}(t_z, \mathbf{z}; \mathbf{z}_d) = \nu_b(t_z, \mathbf{z}) + \nu_t(t_z, \mathbf{z}; \mathbf{z}_d), \quad (65b)$$

where ν_b , ν_t , and ν_s are defined in (47), (55) and (58), respectively, and \mathbf{z}_d in (65a) and (65b) is the same. The names ‘s-model’ and ‘t-model’ are intended to match the terms ‘s-scatterer’ and ‘t-scatterer’ introduced in section 3.2, see (55) and (58). Accordingly, the corresponding total images are given by either

$$I_{\text{s-model}}(t, \mathbf{y}; \mathbf{z}_d) = I_b(t, \mathbf{y}) + I_n(t, \mathbf{y}) + I_s(t, \mathbf{y}; \mathbf{z}_d) \quad (66a)$$

or

$$I_{\text{t-model}}(t, \mathbf{y}; \mathbf{z}_d) = I_b(t, \mathbf{y}) + I_n(t, \mathbf{y}) + I_t(t, \mathbf{y}; \mathbf{z}_d). \quad (66b)$$

In formulae (66), we have introduced the terms I_n to represent the receiver noise and processing errors. The noise I_n is taken as a circular Gaussian process with independent samples. Note that the background I_b is also a circular Gaussian process, but its correlation properties are different—they are determined by the imaging kernel (35), see section 3.1. A detailed definition of the noise term I_n is given in appendix.

Our discrimination procedure will be based on the analysis of the image $I(t_y, \mathbf{y})$. In addition to the image per se, we assume that some *a priori* information is known about the target, such as the reflectivity profiles $F_{s,t}(\zeta)$. We will also assume that we know \mathbf{z}_d . We can find candidate locations for \mathbf{z}_d as the locations of sharp increases in the intensity of a standard SAR image $I(0, \mathbf{y})$ in the range direction. The latter can potentially be identified using edge detection [40–43], a technique that we do not discuss in the current paper.

As long as \mathbf{z}_d is known, we can define the ambiguity lines for inhomogeneous scatterers, see figure 3. To tell between the scatterer types, we would ideally want to obtain a large amount of data. However, the samples of an image given by convolution (14) will not be independent, with the correlation determined by the kernel $W(t_y, \mathbf{y}; t_z, \mathbf{z})$ of (35). The geometry of the central peak and sidelobes of W has been analyzed in section 2.3. From this analysis, we derive that the autocorrelation of $I(t_y, \mathbf{y})$ quickly decreases across the ambiguity directions (section 3.1). For this reason, we will take a finite number of values of ζ_y according to

$$\zeta_{y,m} = \pi m, \quad \eta_m = 0, \quad \text{where } m \in \mathbb{N}, \quad \zeta_{\min} < \zeta_{y,m} \leq \zeta_{\max}. \quad (67)$$

In (67), ζ_{\max} is a parameter of the formulation, see also (63). In addition, we have introduced another parameter, $\zeta_{\min} \gtrsim \pi$, to cut off the transitional effects due to the behavior of $F_s(\zeta)$ and $F_t(\zeta)$ given by (57) in the vicinity of $\zeta = 0$. The set of locations $\{\zeta_{y,m}\}$ given by (67) defines a family of ambiguity lines via (60) such that we can treat the samples of the image taken on different ambiguity lines as independent.

Still, to resolve the range-delay ambiguity, we should take more than one measurement of I on each ambiguity line. In doing so, we cannot avoid dealing with strongly correlated image samples, because the autocorrelation of $I(t_y, \mathbf{y})$ decreases slowly along the ambiguity direction (section 3.1). In this work, for each ambiguity line introduced for $(\zeta_{y,m}, \eta_m)$ of (67), we will take two values of I that correspond to the ambiguity pair ‘S’ and ‘T’, see figure 3. In other words, we will consider a set of pairs $(I_{\text{streak}}^S(\zeta_{y,m}), I_{\text{streak}}^T(\zeta_{y,m}))$:

$$\begin{aligned} I_{\text{streak},m}^S &\stackrel{\text{def}}{=} I(t_y, \mathbf{y}) \Big|_{t_y=0, \mathbf{y}=\mathbf{z}_d + \mathbf{e}_2 \omega_0 \zeta_{y,m} / (Bk_0\theta)}, \\ I_{\text{streak},m}^T &\stackrel{\text{def}}{=} I(t_y, \mathbf{y}) \Big|_{t_y=2\zeta_{y,m}/B, \mathbf{y}=\mathbf{z}_d}, \end{aligned} \quad (68)$$

where $\zeta_{y,m}$ is given by (67). Choosing the locations ‘S’ and ‘T’ on a given ambiguity line has the advantage of maximizing the expectation of the intensity of at least one of the two possible

inhomogeneous images, $|I_s|^2$ or $|I_t|^2$. This is beneficial in the presence of fluctuations due to the background and noise.

In addition to the samples (68) taken at the streak, we would like to see whether sampling the homogeneous part of the image around the streak:

$$I(t_y, \mathbf{y}) = I_b(t_y, \mathbf{y}) + I_n(t_y, \mathbf{y}) \quad (69)$$

may affect the performance of the discrimination algorithm to be built. To that end, we take a set of points $\{\mathbf{y}_k\}$ such that the image values at $(t_y, \mathbf{y}) = (0, \mathbf{y}_k)$ have low correlation with each other and with the streak samples, see (53), and consider the following homogeneous samples

$$\begin{aligned} I_{\text{hom},k}^S &\stackrel{\text{def}}{=} I(t_y, \mathbf{y}) \Big|_{t_y=0, \mathbf{y}=\mathbf{y}_k}, \\ I_{\text{hom},k}^T &\stackrel{\text{def}}{=} I(t_y, \mathbf{y}) \Big|_{t_y=2\zeta_{\text{max}}/B, \mathbf{y}=\mathbf{y}_k - \mathbf{e}_2 \omega_0 \zeta_{\text{max}} / (Bk_{0\theta})}. \end{aligned} \quad (70)$$

Their effect on the discrimination quality is outlined in section 6.

4.3. Anticipated statistics of the sampled image

The second moments of the various image components in (66) can be obtained by substituting the scatterer models ν_b , ν_t , and ν_s (see formulae (50), (56) and (59), respectively) into the imaging operator (14) with the kernel (35). The details of the calculations are given in appendix. The resulting expressions have the following form (see (51) and (61)):

$$\begin{aligned} \langle |I_\alpha^S(\zeta)|^2 \rangle &= \sigma_\alpha^2 K_\alpha G_\alpha^S[F_\alpha](\zeta), \\ \langle |I_\alpha^T(\zeta)|^2 \rangle &= \sigma_\alpha^2 K_\alpha G_\alpha^T[F_\alpha](\zeta), \\ \langle \overline{I_\alpha^T(\zeta)} I_\alpha^S(\zeta) \rangle &= \sigma_\alpha^2 K_\alpha H_\alpha[F_\alpha](\zeta). \end{aligned} \quad (71)$$

In (71), we use the following notations:

- The superscripts S and T are the same as introduced in (68); they refer to the components of an ambiguity pair, see figure 3. A certain fixed value of \mathbf{z}_d is always assumed.
- The subscripts $\alpha \in \{b, t, s\}$ refer to the scatterer models ν_b , ν_t , and ν_s , respectively, whereas $\sigma_{b,t,s}^2$ are the corresponding scattering intensities.
- The operators $G_{b,s,t}^S$, $G_{b,s,t}^T$, and $H_{b,s,t}$ act on the functions $F_{b,s,t}$. These operators, as well as the scalars $K_{b,s,t}$, are defined in appendix.
- The case $\alpha = n$ corresponds to the noise term I_n introduced in (66) and (69). The corresponding intensity σ_n^2 , constant K_n , function $F_n(\zeta)$, and operators $G_n^{S,T}[F_n]$ and $H_n[F_n]$ are also defined in appendix.

Using (71), we express the statistics of the image samples defined by (68) for the case of an instantaneous inhomogeneous target (65a) as follows:

$$\begin{aligned} \text{s-model :} \quad \langle |I_{\text{streak},m}^{S,T}|^2 \rangle &= \sum_{\alpha \in \{b,n,s\}} \sigma_\alpha^2 K_\alpha G_\alpha^{S,T}[F_\alpha](\zeta_{y,m}), \\ \langle \overline{I_{\text{streak},m}^T} I_{\text{streak},m}^S \rangle &= \sum_{\alpha \in \{b,n,s\}} \sigma_\alpha^2 K_\alpha H_\alpha[F_\alpha](\zeta_{y,m}). \end{aligned} \quad (72)$$

For the homogeneous samples (70) we have:

$$\begin{aligned} \langle |I_{\text{hom},k}^{S,T}|^2 \rangle &= \sum_{\alpha \in \{b,n\}} \sigma_\alpha^2 K_\alpha G_\alpha^{S,T}[F_\alpha] (\zeta_{\max}), \\ \text{s-model or t-model : } \langle \overline{I_{\text{hom},k}^T} I_{\text{hom},k}^S \rangle &= \sum_{\alpha \in \{b,n\}} \sigma_\alpha^2 K_\alpha H_\alpha[F_\alpha] (\zeta_{\max}) \end{aligned} \quad (73)$$

For the delayed target (65b), the summation over $\alpha \in \{b, n, s\}$ on the right-hand side of formulae (72) is replaced with the summation over $\alpha \in \{b, n, t\}$:

$$\begin{aligned} \text{t-model : } \langle |I_{\text{streak},m}^{S,T}|^2 \rangle &= \sum_{\alpha \in \{b,n,t\}} \sigma_\alpha^2 K_\alpha G_\alpha^{S,T}[F_\alpha] (\zeta_{y,m}), \\ \langle \overline{I_{\text{streak},m}^T} I_{\text{streak},m}^S \rangle &= \sum_{\alpha \in \{b,n,t\}} \sigma_\alpha^2 K_\alpha H_\alpha[F_\alpha] (\zeta_{y,m}). \end{aligned} \quad (74)$$

4.4. Statistical averages versus individual realizations

The possibility to distinguish between the scatterers described by the t-model (65b) and s-model (65a) is due to the difference in the behavior of the inhomogeneous image components $\langle |I_t^{S,T}(\zeta)|^2 \rangle$ and $\langle |I_s^{S,T}(\zeta)|^2 \rangle$ in the streak data, as explained in section 4.1. Figure 5 plots these averages in panels (a) and (b), respectively, according to formulae (71), (A.16) and (A.20). We see that the plot of $\langle |I^T|^2 \rangle$ (dashed line) lies above $\langle |I^S|^2 \rangle$ (solid line) for the t-model, and vice versa for the s-model. In addition, we plot average values of the same quantities over ensembles of 400 sampled images generated using the Monte-Carlo procedure described in sections 5 and 6 (the data corresponds to the case of $\kappa = 0.4$ and $\zeta_{\max} = 20\pi$ in item A, section 6).

Unlike the experimental averages, individual realizations can deviate quite significantly from the theoretical averages, as shown in figure 5, panels (c) and (d). In each panel, we display two randomly generated realizations, indexed by $j = 1$ and $j = 2$, with the graphs in blue and red colors, respectively. Similarly to panels (a) and (b), the dashed and solid curves correspond to I^T and I^S , respectively. We can see that in panel (c) (t-target), the dashed curves are *above* the solid curves of the same color, similarly to the theoretical averages drawn in black (see also panel (a)). On the contrary, the dashed curves in panel (d) (s-target) are *below* the solid curves of the same color, similarly to panel (b). This is an indication that in the absence of background and noise, we can distinguish between the two types of scatterers on the level of individual images, as discussed following equation (46). Moreover, a single pair of image values taken on one ambiguity line is sufficient to perform the discrimination.

When the background and noise are added to the signals from inhomogeneous scatterers, the plots of the average values look qualitatively the same, as shown in figure 6, panels (a) and (b) (see item A, section 6 for the complete setup). However, there is a very substantial difference compared to figure 5 at the level of individual images, see panels (c) and (d). The curves of the same color are no longer separated vertically, which means that we can randomly observe $|I^T|^2 > |I^S|^2$ or $|I^T|^2 < |I^S|^2$ for either model of the target. In other words, the discrimination between the two models is certain for all plots in figure 5 (no background and noise) and for the top two plots in figure 6 (averages in the presence of background and noise), while it is uncertain for the bottom two plots in figure 6 (individual images with background and noise). In reality however, we can neither exclude the background and noise nor acquire the appropriate statistics. Thus, the discrimination has to be made based on a given image.

A feasible option to increase the reliability of discrimination for the case of individual image in the presence of background and noise is to analyze the image values taken at different ζ . Yet simply comparing the ‘above’ and ‘below’ counts for all available $\zeta_{y,m}$ satisfying (67)

Standalone inhomogeneous scatterers, $\kappa = 0.4$

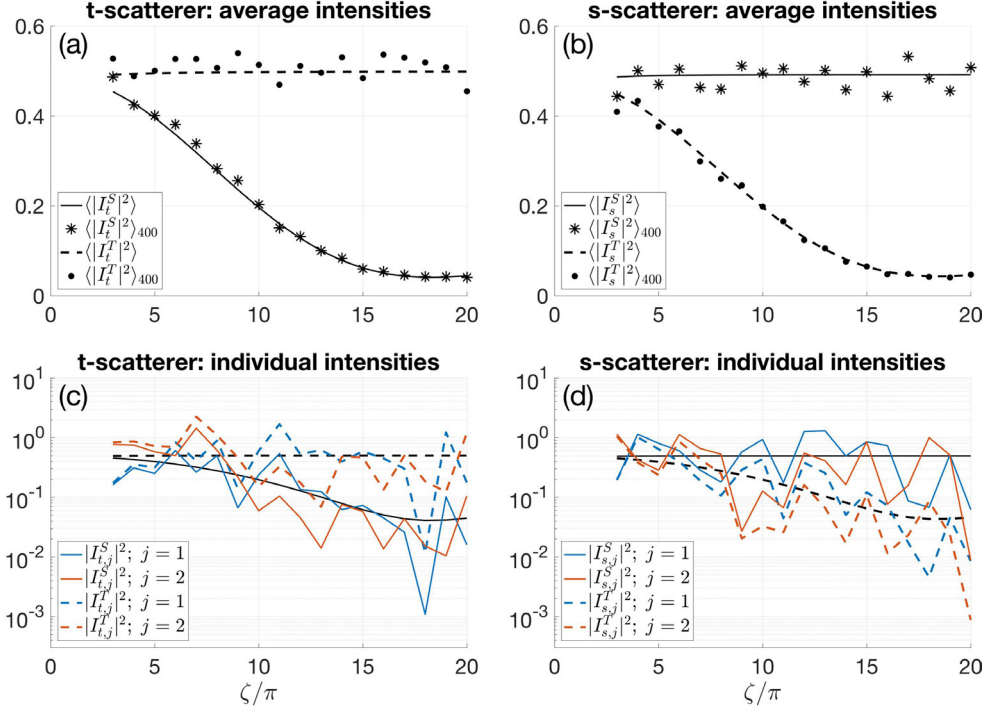


Figure 5. Simulated intensities $I_t^{S,T}$ and $I_s^{S,T}$ of sampled image components due to standalone inhomogeneous scatterers as functions of the non-dimensional time (or range) variable ζ for $\kappa = 0.4$. (a) Scatterer model (55) and (56): the graphs for $\langle |I_t^T(\zeta)|^2 \rangle$ and $\langle |I_t^S(\zeta)|^2 \rangle$ are drawn according to (71) and (A.16), whereas $\langle \cdot \rangle_{400}$ denotes averages over an ensemble of 400 simulated datasets, see sections 5 and 6. (b) Same as (a), but for the scatterer model (58) and (59), see (71) and (A.20). (c) Two randomly generated realizations due to the scatterer model (55) and (56) indexed by $j = 1$ and $j = 2$. The smooth curves are the same as in panel (a), but the logarithmic scale in the ordinate axis is used to accommodate a much larger dynamic range. (d) Same as (c), but for the scatterer model (58) and (59); smooth curves are the same as in (b). Note that the dashed blue and red curves are strictly above the corresponding solid curves in panel (c) and strictly below in panel (d); this can be used to distinguish between the two types of scatterers.

is not sufficient because this procedure ignores the variation of probability of obtaining the ‘incorrect’ relation between $|I^T(\zeta)|^2$ and $|I^S(\zeta)|^2$. This probability increases as $\zeta \rightarrow 0$ because the separation between the expectations (i.e. the curves in panels (a) and (b)) decreases. We therefore employ a likelihood-based discrimination procedure. Not only does it incorporate all available $\zeta_{y,m}$, but also takes into account the probabilities of obtaining each individual value of $I_{\text{streak},m}^{S,T}$ and $I_{\text{hom},k}^{S,T}$ for each of the models in (65).

4.5. Description of the discrimination procedure

The problem of discrimination between the scenarios (65a) and (65b) can now be formulated as follows. For a given image, our dataset consists of two sets of pairs of complex numbers.

Inhomogeneous scatterers with background and noise, $\kappa = 0.4$

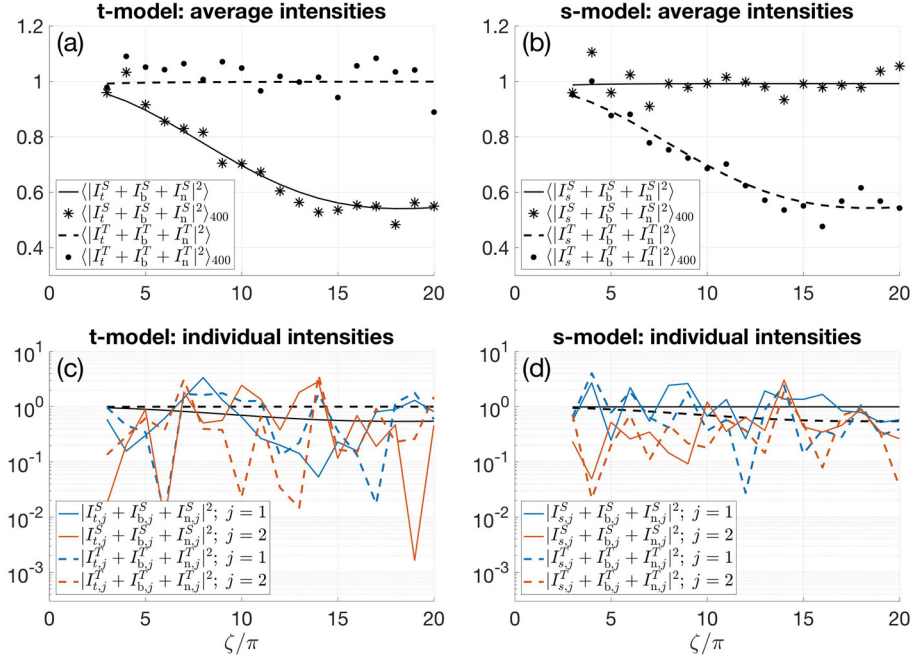


Figure 6. Same as figure 5, but for the total image: $I_t^{S,T} + I_b^{S,T} + I_n^{S,T}$ instead of $I_t^{S,T}$ for panels (a) and (c), see (66b), and $I_s^{S,T} + I_b^{S,T} + I_n^{S,T}$ instead of $I_s^{S,T}$ for panels (b) and (d), see (66a). The graphs in panels (a) and (b) are drawn according to the top formulae in (74) and (72), respectively, with the scatterer intensities $\sigma_\alpha^2 K_\alpha$ defined in section 6 with the help of (88). Note that in the presence of the background I_b and noise I_n , the curves of the same color in panels (c) and (d) cross-cut one another, unlike in figure 5. This means that the discrimination between the two types of target models based on the measurements for a single value of ζ cannot be robust.

There are streak pairs $(I_{\text{streak},m}^S, I_{\text{streak},m}^T)$ given by (68), where $1 \leq m \leq N_{\text{streak}}$ and N_{streak} is determined by (67). In addition, there are homogeneous pairs $(I_{\text{hom},k}^S, I_{\text{hom},k}^T)$ given by (70), where $1 \leq k \leq N_{\text{hom}}$ and N_{hom} is a parameter of the formulation. We also have two mathematical models for the statistics of these pairs. The first model is given by (72) and (73), whereas the second model is given by (73) and (74). These models contain the unknown parameters σ_s^2 and σ_t^2 , respectively. Moreover, they share two common unknowns σ_b^2 and σ_n^2 . The problem of discrimination is to choose the model that fits the given dataset better than the other model does.

For each of the two models, our discrimination algorithm will seek the set of unknowns σ_α^2 that maximizes the probability density of the dataset. Then, we will choose the model that yields the larger of the two maxima. This is the same idea as that behind the maximum likelihood (ML) approach [9, 44].

For a given scatterer type α , let \mathbf{r} be a vector of four real Gaussian random variables that define the quantities on the left-hand side of (71):

$$\mathbf{r} \stackrel{\text{def}}{=} (\text{Re } I_\alpha^S(\zeta), \text{Im } I_\alpha^S(\zeta), \text{Re } I_\alpha^T(\zeta), \text{Im } I_\alpha^T(\zeta))^T. \quad (75)$$

Introduce the following brief notations for the right-hand sides of (71):

$$\begin{aligned} A &= \sigma_\alpha^2 K_\alpha G_\alpha^S[F_\alpha](\zeta), & C &= \operatorname{Re}(\sigma_\alpha^2 K_\alpha H_\alpha[F_\alpha](\zeta)), \\ B &= \sigma_\alpha^2 K_\alpha G_\alpha^T[F_\alpha](\zeta), & D &= \operatorname{Im}(\sigma_\alpha^2 K_\alpha H_\alpha[F_\alpha](\zeta)), \end{aligned} \quad (76)$$

so that

$$\langle |I_\alpha^S(\zeta)|^2 \rangle = A, \quad \langle |I_\alpha^T(\zeta)|^2 \rangle = B, \quad \langle \overline{I_\alpha^T(\zeta)} I_\alpha^S(\zeta) \rangle = C + iD. \quad (77)$$

We have $A, B, C, D \in \mathbb{R}$ and $A, B > 0$. Recall that I_α^S and I_α^T are circular Gaussian variables satisfying $\langle I_\alpha^T(\zeta) I_\alpha^S(\zeta) \rangle = 0$, see (51a). Then, we have

$$\langle \mathbf{r} \mathbf{r}^T \rangle = \frac{1}{2} \begin{pmatrix} A & 0 & C & -D \\ 0 & A & D & C \\ C & D & B & 0 \\ -D & C & 0 & B \end{pmatrix} \stackrel{\text{def}}{=} \mathbf{M}. \quad (78)$$

The condition that the matrix \mathbf{M} is positive semidefinite translates into $AB \geq C^2 + D^2$, or $G_\alpha^S[F_\alpha](\zeta) \cdot G_\alpha^T[F_\alpha](\zeta) \geq |H_\alpha[F_\alpha](\zeta)|^2$. The latter is a consequence of the Schwartz inequality applied to (77).

Next, we switch to the extended notation by adding the indices α and j to \mathbf{r} , A , B , C , D , and \mathbf{M} :

$$(\mathbf{r}, A, B, C, D, \mathbf{M}) \mapsto (\mathbf{r}_{\alpha,j}, A_{\alpha,j}, B_{\alpha,j}, C_{\alpha,j}, D_{\alpha,j}, \mathbf{M}_{\alpha,j}),$$

where α denotes the scatterer type as in (71), and j indexes all pairs of samples in the dataset going first through the streak samples (68) and then through the homogeneous samples (70), so that $1 \leq j \leq (N_{\text{streak}} + N_{\text{hom}})$. In addition, define ζ_j as follows:

$$\zeta_j = \begin{cases} \zeta_{\mathbf{r}, (j + \lfloor \zeta_{\min}/\pi \rfloor)}, & \text{see (67), if } 1 \leq j \leq N_{\text{streak}}, \\ \zeta_{\max}, & \text{otherwise,} \end{cases}$$

where $\lfloor \cdot \rfloor$ denotes the integer part. Accordingly, equations (75) and (76) become:

$$\begin{aligned} \mathbf{r}_{\alpha,j} &\stackrel{\text{def}}{=} (\operatorname{Re} I_\alpha^S(\zeta_j), \operatorname{Im} I_\alpha^S(\zeta_j), \operatorname{Re} I_\alpha^T(\zeta_j), \operatorname{Im} I_\alpha^T(\zeta_j))^T, \\ A_{\alpha,j} &\stackrel{\text{def}}{=} \langle |I_\alpha^S(\zeta_j)|^2 \rangle = \sigma_\alpha^2 K_\alpha G_\alpha^S[F_\alpha](\zeta_j), \end{aligned}$$

and similarly for $B_{\alpha,j}$, $C_{\alpha,j}$, and $D_{\alpha,j}$. Then, introduce

$$(\mathbf{r}_j, A_j, B_j, C_j, D_j, \mathbf{M}_j)_{\text{s-model}} = \sum_{\alpha \in \mathcal{S}_j} (\mathbf{r}_{\alpha,j}, A_{\alpha,j}, B_{\alpha,j}, C_{\alpha,j}, D_{\alpha,j}, \mathbf{M}_{\alpha,j}) \quad (79a)$$

and

$$(\mathbf{r}_j, A_j, B_j, C_j, D_j, \mathbf{M}_j)_{\text{t-model}} = \sum_{\alpha \in \mathcal{T}_j} (\mathbf{r}_{\alpha,j}, A_{\alpha,j}, B_{\alpha,j}, C_{\alpha,j}, D_{\alpha,j}, \mathbf{M}_{\alpha,j}), \quad (79b)$$

where according to (66) and (69), the summation sets \mathcal{S}_j and \mathcal{T}_j are:

$$\mathcal{S}_j = \begin{cases} \{\mathbf{b}, \mathbf{n}, \mathbf{s}\} & \text{for } 1 \leq j \leq N_{\text{streak}}, \\ \{\mathbf{b}, \mathbf{n}\} & \text{for } j > N_{\text{streak}}, \end{cases} \quad \mathcal{T}_j = \begin{cases} \{\mathbf{b}, \mathbf{n}, \mathbf{t}\} & \text{for } 1 \leq j \leq N_{\text{streak}}, \\ \{\mathbf{b}, \mathbf{n}\} & \text{for } j > N_{\text{streak}}. \end{cases}$$

Since different image components given by $\mathbf{r}_{\alpha,j}$ for different α are assumed independent, the moments of the entire \mathbf{r}_j for a fixed j and either of the two models, s-model or t-model, can

be obtained by summing up the moments of the corresponding individual components given by (77) and (78):

$$\begin{aligned}\langle \mathbf{r}_{j, \text{s-model}} \mathbf{r}_{j, \text{s-model}}^T \rangle &= \mathbf{M}_{j, \text{s-model}} = \sum_{\alpha \in \mathcal{S}_j} \mathbf{M}_{\alpha, j}, \\ \langle \mathbf{r}_{j, \text{t-model}} \mathbf{r}_{j, \text{t-model}}^T \rangle &= \mathbf{M}_{j, \text{t-model}} = \sum_{\alpha \in \mathcal{T}_j} \mathbf{M}_{\alpha, j}.\end{aligned}\quad (80)$$

Then, the probability density of \mathbf{r}_j for either of the two models is given by the standard formula for multivariate Gaussian distribution:

$$p(\mathbf{r}_j) = \frac{1}{((2\pi)^4 \det \mathbf{M}_j)^{1/2}} \exp\left(-\frac{1}{2} \mathbf{r}_j^T \mathbf{M}_j^{-1} \mathbf{r}_j\right). \quad (81)$$

The vector \mathbf{r}_j and the matrix \mathbf{M}_j in (81) must correspond to one and the same model, the s-model or t-model, see (80).

The overall vector \mathbf{R} combines all vectors \mathbf{r} of (75) for the streak and homogeneous pairs of samples:

$$\mathbf{R} = \left(\mathbf{r}_1^T, \mathbf{r}_2^T, \dots, \mathbf{r}_j^T, \dots, \mathbf{r}_{N_{\text{streak}}+N_{\text{hom}}}^T \right)^T. \quad (82)$$

As we consider each pair of samples independent, we have:

$$p(\mathbf{R}) = \prod_{j=1}^{N_{\text{streak}}+N_{\text{hom}}} p(\mathbf{r}_j), \quad (83)$$

where individual $p(\mathbf{r}_j)$ are given by (81) for either the s-model or t-model.

Let us now denote by \mathbf{Q} the actual dataset vector that represents a given image. The vector \mathbf{Q} has the same structure as the vector \mathbf{R} of (82):

$$\mathbf{Q} = \left(\mathbf{q}_1^T, \mathbf{q}_2^T, \dots, \mathbf{q}_j^T, \dots, \mathbf{q}_{N_{\text{streak}}+N_{\text{hom}}}^T \right)^T. \quad (84)$$

The individual sub-vectors \mathbf{q}_j in (84) correspond to the samples of the given image taken as described in section 4.2. Each \mathbf{q}_j represents one ambiguity pair and has four real-valued components arranged the same way as in (75).

The vector \mathbf{Q} will provide the input for the discrimination procedure whose primary task is to tell whether it corresponds to an instantaneous or delayed target. The discrimination will be rendered by seeing whether the data \mathbf{Q} fit better the s-model or the t-model, respectively.

In addition to the input data \mathbf{Q} , the discrimination procedure uses the values of ζ_j that are known. The functions A_j , B_j , C_j , and D_j are known for both the s-model and t-model up to the factors σ_α^2 , $\alpha \in \mathcal{S}_j$ or $\alpha \in \mathcal{T}_j$, that are not known, see (76) and (79). It is these factors that are used as optimization variables in order to achieve the best fit between the data and the model.

For a given dataset \mathbf{Q} of (84), consider the two likelihood functions [44] defined via (80), (81), and (83) for the two models that we have built:

$$p_{\text{s-model}}(\mathbf{Q}) = \prod_{j=1}^{N_{\text{streak}}+N_{\text{hom}}} \frac{1}{((2\pi)^4 \det \mathbf{M}_{j, \text{s-model}})^{1/2}} \exp\left(-\frac{1}{2} \mathbf{q}_j^T \mathbf{M}_{j, \text{s-model}}^{-1} \mathbf{q}_j\right), \quad (85a)$$

$$p_{t\text{-model}}(\mathbf{Q}) = \prod_{j=1}^{N_{\text{streak}}+N_{\text{hom}}} \frac{1}{((2\pi)^4 \det \mathbf{M}_{j,t\text{-model}})^{1/2}} \exp\left(-\frac{1}{2} \mathbf{q}_j \mathbf{T} \mathbf{M}_{j,t\text{-model}}^{-1} \mathbf{q}_j\right). \quad (85b)$$

The functions $p_{s\text{-model}}$ and $p_{t\text{-model}}$ of (85) depend on the unknown intensities σ_α^2 that appear in the entries of the matrices $\mathbf{M}_{j,s\text{-model}}$ and $\mathbf{M}_{j,t\text{-model}}$, see formulae (76), (78), and (80). The discrimination procedure solves two optimization problems formulated as follows:

$$\check{p}_s = \max_{\sigma_b^2, \sigma_n^2, \sigma_s^2} p_{s\text{-model}}(\mathbf{Q}), \quad \check{p}_t = \max_{\sigma_b^2, \sigma_n^2, \sigma_t^2} p_{t\text{-model}}(\mathbf{Q}), \quad (86)$$

subject to $\sigma_b^2, \sigma_n^2, \sigma_s^2, \sigma_t^2 \geq 0$, where $p_{s\text{-model}}(\mathbf{Q})$ and $p_{t\text{-model}}(\mathbf{Q})$ are defined by (85a) and (85b), respectively. The resulting \check{p}_s and \check{p}_t yield the maximum likelihood (ML) values for the corresponding scatterer models. The classification decision, i.e. the discrimination, is made by comparing the two maxima:

$$\begin{aligned} &\text{if } \check{p}_t > \check{p}_s \\ &\text{then} \\ &\quad \text{the target is classified as a delayed scatterer (65b), (66b)} \\ &\text{else} \\ &\quad \text{the target is classified as an instantaneous scatterer (65a), (66a).} \end{aligned} \quad (87)$$

In other words, algorithm (87) attributes a given target to one of the two possible types based on whether $\check{p}_t > \check{p}_s$ or $\check{p}_t < \check{p}_s$. Thus, the issue of confidence intervals becomes important, especially in the presence of noise. Suppose, for example, that $\check{p}_t > \check{p}_s$. Then, how much of a gap shall we have between \check{p}_t and \check{p}_s to be confident that the classification of the target as a delayed scatterer is correct? This question will be addressed in the future.

5. Performance analysis of the discrimination procedure

To assess the performance of the discrimination procedures of section 4.5, we will simulate a large number of image vectors (82) using both models in (66), substitute the simulated vectors \mathbf{R} for \mathbf{Q} and thus generate the datasets (84), run algorithm (87) on each of the datasets, and count the number of correct and incorrect classifications. As there is usually only one image available for analysis, the discrimination algorithm is not allowed to ‘learn’ from the resulting statistics. It does not know either which of the two models has been used to obtain a given vector (82) and what the corresponding values of σ_α^2 were.

A block diagram for performance assessment is shown in figure 7. An ensemble of sampled coordinate-delay SAR images represented by datasets (84) is generated using the Monte-Carlo method. We start with choosing $F_{s,t}(\zeta)$, ζ_{\min} , ζ_{\max} , κ , and N_{hom} . The relative scatterer intensities, or contrasts, are defined as follows:

$$p_n = \frac{\sigma_n^2 K_n}{\sigma_b^2 K_b}, \quad q_{st} = \frac{\sigma_s^2 K_s}{\sigma_s^2 K_s + \sigma_b^2 K_b + \sigma_n^2 K_n} = \frac{\sigma_t^2 K_t}{\sigma_t^2 K_t + \sigma_b^2 K_b + \sigma_n^2 K_n}. \quad (88)$$

This allows us to calculate $\sigma_s^2 K_s$, $\sigma_t^2 K_t$, $\sigma_b^2 K_b$, and $\sigma_n^2 K_n$ accurate to a common factor. Note that we always take the $\sigma_s^2 K_s = \sigma_t^2 K_t$, which makes sense from the standpoint of the discrimination problem. For example, if the range-delay ambiguity is not resolved, then the statistical properties of the instantaneous and delayed images will be the same, see (71).

Each dataset consists of the streak data and homogeneous data, as per section 4.3. To create the streak data, we generate a pair of circular Gaussian pseudo-random variables

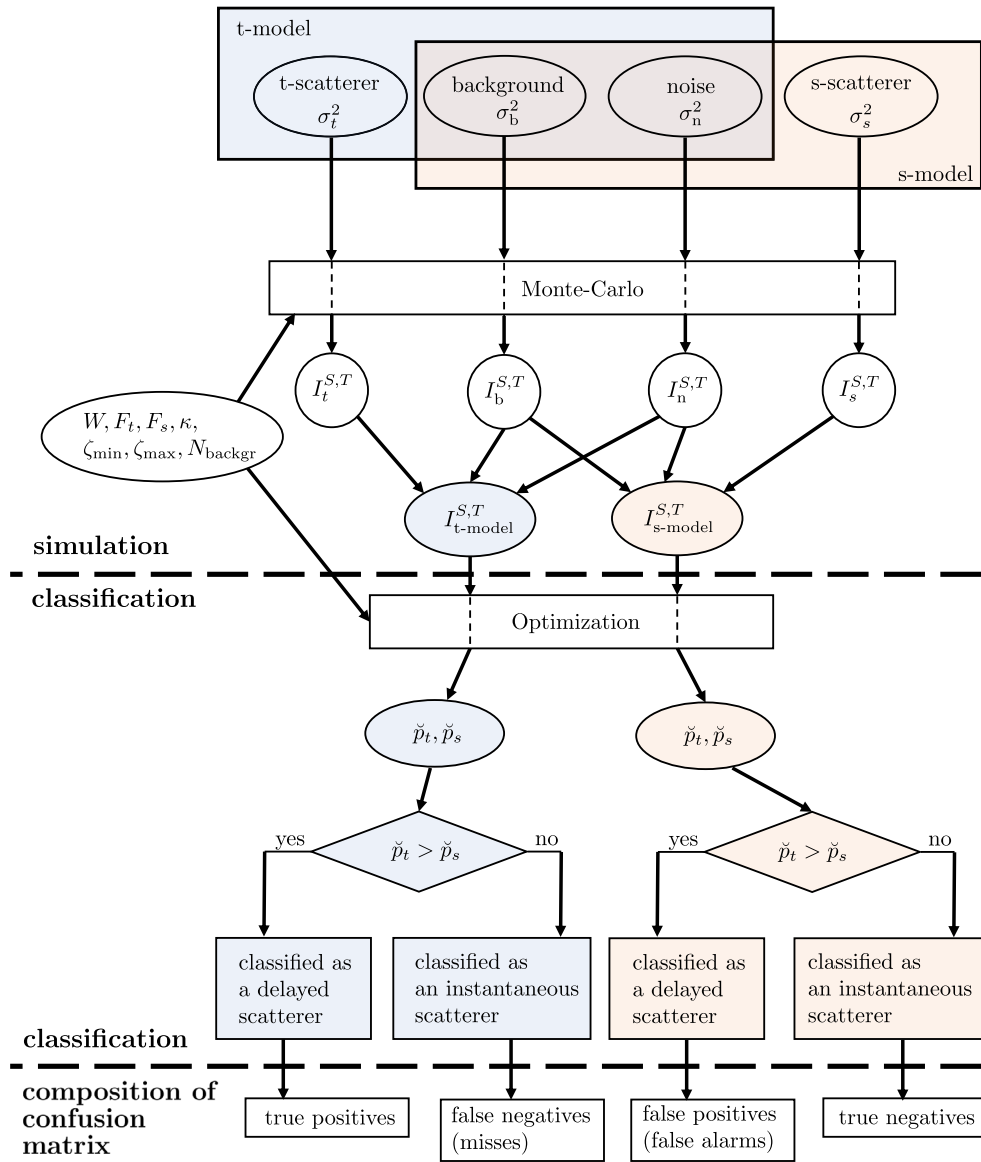


Figure 7. Performance analysis of the discrimination procedure.

$(I_\alpha^S(\zeta_y), I_\alpha^T(\zeta_y))$ for each ζ_y that satisfies (67) and each $\alpha \in \{b, n, s, t\}$, with the moments given by (71), see also appendix and examples in figures 5(c) and (d). Then we compute the sum of the resulting pairs $(I_\alpha^S(\zeta_y), I_\alpha^T(\zeta_y))$ according to (66a) and (66b) for scenarios (65a) and (65b), respectively, and obtain the samples (68), see examples in figures 6(c) and (d). For the homogeneous data, we generate N_{hom} of pseudo-random pairs $(I_b^S(\zeta_{\max}), I_b^T(\zeta_{\max}))$ and $(I_n^S(\zeta_{\max}), I_n^T(\zeta_{\max}))$ and compute the sums according to (69) to obtain the samples (70). We combine the streak data with the homogeneous data for each of the two target models in (66) and obtain two vectors \mathbf{R} of (82). The discrimination procedure treats them as two datasets \mathbf{Q}

Table 1. Confusion matrix: the entries are relative frequencies of events.

	Output: s	Output: t
Input: s	$1 - r_s$	r_s
Input: t	r_t	$1 - r_t$

of (84), each consisting of $2(N_{\text{streak}} + N_{\text{hom}})$ complex numbers. These datasets represent one image for each of the two target models given in (65).

By repeating the foregoing procedure N_{img} times, we obtain an ensemble of $2N_{\text{img}}$ ‘images’ (i.e. datasets). It consists of two sub-ensembles, of N_{img} images each, generated using one of the two target models in (65). After an ensemble has been generated, each image goes through the discrimination procedure, see section 4.5, and is classified as either an instantaneous (i.e. originating from the s-model) or delayed (t-model) scatterer, see (87). The classification outcome contributes to one of the four cells in table 1, which is called the confusion matrix [45]. Rows of table 1 are determined by the actual scatterer type or, in our case, by the underlying model used to generate the dataset. Columns of table 1 are determined by the classification result. The data in table 1 are normalized by N_{img} .

An ideal confusion matrix would be diagonal; in other words, having $r_s = r_t = 0$. If our goal is to detect delayed targets, then, e.g. r_s can be identified as the false alarm ratio, see figure 7. The performance of the discrimination procedure can be expressed via the values of error frequencies r_s and r_t . The quality of discrimination may depend on the scene and processing parameters, e.g. on ζ_{max} , N_{hom} , κ , target parametrization, contrasts, sampling, etc; some of these dependencies are demonstrated in section 6.

Note that the values r_s and r_t calculated using Monte-Carlo simulation are random, and hence, as metrics of the discrimination quality, contain some errors because of the finite size of the ensemble. Assuming $\langle r_s \rangle$ and $\langle r_t \rangle$ to be the true (and unknown) error frequencies, we find that each row in table 1 contains the averages due to the binomial distribution. Then, we have [44]:

$$\text{std}(r_s) = \left(\frac{\langle r_s \rangle \cdot (1 - \langle r_s \rangle)}{N_{\text{img}}} \right)^{1/2}, \quad \text{std}(r_t) = \left(\frac{\langle r_t \rangle \cdot (1 - \langle r_t \rangle)}{N_{\text{img}}} \right)^{1/2}. \quad (89)$$

Hence, for large N_{img} the error frequencies $\langle r_s \rangle$ and $\langle r_t \rangle$ can be approximated by their estimates r_s and r_t , respectively.

6. Results of simulations

We have tested the discrimination between instantaneous and delayed targets using the methodology presented in sections 4.5 and 5. Our goal was to see how the change of various problem parameters affects the quality of discrimination in percentage points defined as

$$\text{round} \left[100\% \cdot \left(1 - \frac{r_s + r_t}{2} \right) \right], \quad (90)$$

see table 1. With $N_{\text{img}} = 400$, each Monte-Carlo run generates an ensemble consisting of 800 ‘images’ for calculation of the discrimination quality metrics presented in table 1. Note that according to (89), the stochastic errors of metric (90) can be of the order of $100\% / (2\sqrt{N_{\text{img}}}) = 2.5\%$.

The generic parameters of the simulations are: $\zeta_{\text{min}} = 3\pi$, $\zeta_{\text{max}} = 12\pi$ (so that $N_{\text{streak}} = 10$), $N_{\text{hom}} = 15$; the relative contrasts defined in (88) are $p_n = 0.25$ and $q_{st} = 0.4$. In

each particular Monte-Carlo run, some of these parameters could vary. Our numerical simulations are as follows.

- (A) To see how the discrimination quality depends on ζ_{\max} , we generated three image ensembles with $\zeta_{\max} = 4\pi$, 8π , and 20π . For $\kappa = 0.4$, this case is illustrated in figures 5 and 6. The corresponding quality metrics (90) were 52%, 66% and 94% for $\kappa = 0.4$, and 64%, 83% and 98% for $\kappa = 1$. Note that condition $\kappa\zeta_{\max} > b_{\Phi}$, see (64), is not satisfied for the first two runs for $\kappa = 0.4$ and the first run for $\kappa = 1$. Altogether, the discrimination quality improves with the increase of $\kappa\zeta_{\max}$. Note that such increase simultaneously affects the number of samples in the inhomogeneous area, i.e. N_{streak} , and the average separation between the theoretical curves in figure 6, panels (a) and (b) (see top formulae in (74) and (72)). In items B and C, we investigate the corresponding effects separately.
- (B) To demonstrate the advantage of taking multiple $\zeta_{y,m}$ (i.e. multiple delays) in the streak data, see (68), we set up three ensembles with $\zeta_{\min} = 3\pi$, 8π , and 12π , such that $N_{\text{streak}} = 10$, 5, and 1, while $\zeta_{\max} = 12\pi$. The corresponding quality metrics (90) were 78%, 73% and 63% for $\kappa = 0.4$, and 89%, 77% and 65% for $\kappa = 1$. Note that for the case $N_{\text{streak}} = 1$ and $\kappa\zeta_{\max}/b_{\Phi} = 1 \cdot 12\pi/b_{\Phi} \approx 1.6$, where condition (64) is satisfied with a significant margin, about a third of discrimination results are still incorrect. We consider this case as representing the ‘deterministic’ approach to discrimination (as outlined in section 2) because only a single sample of the scattering delay is taken.
- (C) To refine the interpretation of the results in item A further, we ran another test where we varied ζ_{\max} while keeping N_{streak} constant. In particular, we took $\zeta_{\max} = 10\pi$, 20π , and 40π , and $N_{\text{streak}} = 6$. The corresponding quality metrics (90) were 52%, 69% and 85% for $\kappa = 0.15$, 69%, 84% and 87% for $\kappa = 0.4$, and 83%, 84% and 88% for $\kappa = 1$. While the effect due to ζ_{\max} is clear for $\kappa = 0.15$, we can observe some saturation in the response of the discrimination quality to the increase of $\kappa\zeta_{\max}$ if N_{streak} remains constant. Together with items A and B, this reinforces the importance of including multiple values of $\zeta_{y,m}$ into the analysis.
- (D) We varied the target contrast q_{st} , see (88), by setting its values to 0.1, 0.3, and 0.6. The intensity of the background was adjusted accordingly so that the relative intensity of noise always remained 0.1, i.e. $p_n = 0.1/(0.9 - q_{st})$. The corresponding quality metrics (90) were 53%, 65% and 83% for $\kappa = 0.4$, and 57%, 71% and 95% for $\kappa = 1$. Obviously, discrimination of low-contrast targets is less reliable than that of high-contrast targets.
- (E) The number of homogeneous pairs of samples (70) did not noticeably affect the quality of discrimination. We have tried various combinations of parameters, including $N_{\text{hom}} = 0$, and the effect never exceeded 5%.

7. Discussion

We have demonstrated a functioning methodology of distinguishing between delayed and instantaneous scatterers in coordinate-delay SAR images. To make this approach more practical, several issues still need to be addressed.

- Testing the discrimination of targets against an inhomogeneous or textured background [9] and with delayed and inhomogeneous targets having non-singular support of the reflectivity function (see (55) and (58)).
- Fully taking into account the correlation between image samples rather than restricting it to (S,T)-pairs as explained in section 4.3. This opens a venue to increasing the number of samples taken from each image.
- Obtaining the confidence level for a given discrimination.

- Automatic selection of the reference target position \mathbf{z}_d . The coordinates z_{d1}, z_{d2} may be included into the set of optimization variables in (86).
- Testing the discrimination method on a broader set of functions $F_t(\zeta)$ and $F_s(\zeta)$. In particular, these function may correspond to certain physical mechanisms of delayed scattering, including the cases where the actual returned signal has a deterministic component. Examples of such mechanisms can be the Foldy-Lax dispersion model, see [46, section 9.9], or the waveguide model of [13].
- Developing an efficient numerical methodology for obtaining the coordinate-delay SAR images from raw radar data, as given by the first sum in (13). Matched filtering/back-projection methods are computationally demanding because both range and azimuthal sums typically contain on the order of 10^3 terms for each pixel. The existing algorithms for standard SAR processing, such as the Range Doppler or Chirp Scaling, use fast Fourier transform (FFT) to accelerate the computation of a large number of convolutions [10, part II]. The coordinate-delay image $I(t_y, \mathbf{y})$ will have many more ‘pixels’ than the standard image $I_{\text{std}}(\mathbf{y}) = I(0, \mathbf{y})$, so the benefits of using FFT may be even more apparent. Moreover, parallel numerical algorithms on multi-processor or multi-core architectures (e.g. GPUs) enable further reduction of computational costs in SAR processing, see, e.g. [47].

Note that the discrimination procedure assumes a certain form of the functions $F_t(\zeta)$ in (56) and $F_s(\zeta)$ in (59), see, e.g. (57). For testing, we generated the data that matched the assumptions built into the discrimination algorithm (see section 5). In practice, this may be the case if we have some *a priori* knowledge about the possible target.

However, in real applications we may have to deal with the targets characterized by $F_t(\zeta)$ or $F_s(\zeta)$ that are not known to the remote system. If these functions differ significantly from those used in the discrimination procedure, then the optimization problems (86) lose their relevance. To remedy this situation, one can represent $F_{s,t}(\zeta)$ as expansions with respect to a specially chosen basis $\{F_i(\zeta)\}$. As the functionals $G_\alpha^{S,T}$ and H_α are linear, see appendix, equations (71) will change according to

$$\begin{aligned} \sigma_\alpha^2 G_\alpha^{S,T}[F_\alpha](\zeta) &\mapsto \sum_{i=1}^M \sigma_{\alpha,i}^2 G_\alpha^{S,T}[F_i](\zeta), \\ \sigma_\alpha^2 H_\alpha[F_\alpha](\zeta) &\mapsto \sum_{i=1}^M \sigma_{\alpha,i}^2 H_\alpha[F_i](\zeta), \end{aligned} \tag{91}$$

where the basis functions $F_i(\zeta)$ are known. Then, each unknown σ_α^2 in the optimization problems will be replaced with M expansion coefficients, $\sigma_{\alpha,i}^2$, while the rest of the procedure remains the same.

The choice of the basis $\{F_i(\zeta)\}$ and its dimension M is central for the approach (91). The case we considered in this paper is $M = 1$ and $F_1(\zeta)$ given by (57). By increasing M and properly selecting F_i , we can fit the unknown functions F_s and F_t better. As, however, indicated in section 4.2, the sampling rate w.r.t. ζ_y in the streak data is bounded from below, see (67). Hence, there are only finitely many samples $F_s(\zeta_{y,m})$ and $F_t(\zeta_{y,m})$, and choosing $M \geq N_{\text{streak}}$ will imply overfitting. We leave this and related topics (e.g. whether we should require $\sigma_{\alpha,i}^2 \geq 0$ for all α and i) for a future study.

An even more serious modification of the current approach may be required to accommodate the wide-angle and full circular apertures, where the reflectivity in (1) can no longer be considered independent of \mathbf{x} , or delays smaller than $1/B$ that make the streak shorter than one pixel in range, see figure 3.

Acknowledgments

We would like to thank Profs M Cheney (Colorado State University) and A Doerry (University of New Mexico; Sandia) for fruitful discussions. This material is based upon work supported by the US Air Force Office of Scientific Research (AFOSR) under awards number FA9550-14-1-0218 and FA9550-17-1-0230. The first author also acknowledges support by the National Science Foundation under Grant No. DMS-1439786 while he was in residence at the Institute for Computational and Experimental Research in Mathematics (Brown University, Providence, RI) during the Fall Semester of 2017.

Appendix. Second moments of image components

Here we calculate the right hand sides of (71) for different scatterer types denoted by α . We need to recall formula (14) for the image:

$$I(t_y, \mathbf{y}) = \int_0^\infty dt_z \int d\mathbf{z} \nu(t_z, \mathbf{z}) W(t_y, \mathbf{y}; t_z, \mathbf{z}), \quad (\text{A.1})$$

and expression (45) for the imaging kernel

$$W(t_y, \mathbf{y}; t_z, \mathbf{z}) = N\tau \exp\left(-2i\frac{\omega_0}{B}\zeta\right) \cdot \Phi(\eta, \kappa(\zeta - B(t_y - t_z)/2)) \cdot \text{sinc } \zeta, \quad (\text{A.2})$$

where

$$\kappa = \varphi_T^2 \frac{\omega_0}{B}, \quad \eta = k_{0\theta} \varphi_T (y_1 - z_1), \quad \zeta = \frac{B}{\omega_0} k_{0\theta} (y_2 - z_2) + B \frac{t_y - t_z}{2},$$

see (40) and (44). In what follows, we will use these expressions with different formulations for $\nu(t_z, \mathbf{z})$.

To simplify calculations, functions $F_t(\zeta)$ and $F_s(\zeta)$ in this appendix are taken as $F_t(\zeta) = F_s(\zeta) = (1 + \text{sign}\zeta)/2$ rather than the indicator function (57), while ζ_{\max} in sections 4.2 and 6 acts as a parameter of sampling. Similarly to section 4.1 (see discussion around (61) and (62)), as long as we take $\zeta_{\max} \gg \pi$, which is true for all cases considered in section 6, the effect on the values of integrals in this appendix is insignificant.

A.1. Homogeneous scatterer $\nu_b(t_z, \mathbf{z})$ in (47)–(50)

$$\nu(t_z, \mathbf{z}) = \nu_b(t_z, \mathbf{z}) = \delta(t_z) \mu_b(\mathbf{z}), \quad \langle \overline{\mu_b(\mathbf{z}_a)} \mu_b(\mathbf{z}_b) \rangle = \sigma_b^2 \delta(\mathbf{z}_a - \mathbf{z}_b). \quad (\text{A.3})$$

Substituting (A.3) into (A.1)–(A.2), we obtain

$$I_b(t_y, \mathbf{y}) = N\tau \int \mu_b(\mathbf{z}) \exp\left(-2i\frac{\omega_0}{B}\zeta_0\right) \text{sinc } \zeta_0 \Phi(\eta, \kappa\zeta_0) d\mathbf{z}, \quad (\text{A.4})$$

where $\zeta_0 = \zeta|_{t_z=0}$.

Replacing t_y with a dimensionless argument

$$\zeta_y = B t_y / 2, \quad (\text{A.5})$$

using the delta functions in (A.3), and performing a change of integration variables, we can obtain

$$\langle |I_b(\zeta_y, \mathbf{y})|^2 \rangle = \sigma_b^2 \cdot N^2 \tau^2 \frac{\omega_0}{Bk_{0\theta}} \frac{1}{k_{0\theta} \varphi_T} \cdot \int d\zeta_0 \operatorname{sinc}^2 \zeta_0 \int d\eta \left| \Phi(\eta, \kappa(\zeta_0 - \zeta_y)) \right|^2. \quad (\text{A.6})$$

Obviously, the expression on the right hand side does not depend of \mathbf{y} . A less expected result is that it does not depend on t_y (or ζ_y) either. In order to prove the latter statement, we notice that expression (32) can be formally considered as a Fourier transform $s \leftrightarrow v_1$:

$$\Phi(v_1, v_2) = \int_{-1/2}^{1/2} \exp(2iv_1 s) \exp(iv_2 s^2) ds = \mathcal{F}[\Psi_{v_2}(s)](2v_1),$$

where $\Psi_{v_2}(s) = \exp(iv_2 s^2) \chi_1(s)$,

and the indicator function χ_1 is defined similarly to χ_τ in (17). Then, due to the Parseval's theorem, we have the following identity:

$$\begin{aligned} \int \Phi(\eta, a) \overline{\Phi(\eta, b)} d\eta &= \pi \int \Psi_a(s) \overline{\Psi_b(s)} ds \\ &= \pi \int_{-1/2}^{1/2} \exp(i(a-b)s^2) ds = \pi \Phi(0, a-b). \end{aligned} \quad (\text{A.7})$$

Formula (A.7) immediately evaluates the interior integral in (A.6) to π , and then the outer integral yields another π . Hence, formula (A.6) reduces to

$$\langle |I_b|^2 \rangle = \sigma_b^2 K_b, \quad \text{where} \quad K_b = N^2 \tau^2 \frac{\omega_0}{Bk_{0\theta}} \frac{1}{k_{0\theta} \varphi_T} \cdot \pi^2. \quad (\text{A.8})$$

Using definitions (68) for I^S and I^T and taking an arbitrary \mathbf{z}_d , we write the following expression for the cross-correlation:

$$\begin{aligned} \langle I_b^S(\zeta_y) \overline{I_b^T(\zeta_y)} \rangle &= \sigma_b^2 \cdot N^2 \tau^2 \frac{\omega_0}{Bk_{0\theta}} \frac{1}{k_{0\theta} \varphi_T} \cdot \int d\zeta_0 \operatorname{sinc}^2 \zeta_0 \\ &\quad \cdot \int d\eta \Phi(\eta, \kappa \zeta_0) \overline{\Phi(\eta, \kappa(\zeta_0 - \zeta_y))}. \end{aligned} \quad (\text{A.9})$$

Applying once again formula (A.7) to the interior integral in (A.9), we obtain $\pi \Phi(0, \kappa \zeta_y)$, and, likewise, the outer integration can then be performed. Altogether, from (A.6) and (A.9), in notations of (71) and taking into account (A.8), we write

$$G_b^S[F_b](\zeta) = G_b^T[F_b](\zeta) = 1, \quad H_b[F_b](\zeta) = \Phi(0, \kappa \zeta), \quad (\text{A.10})$$

where F_b may be formally defined as $F_b(\zeta) \equiv 1$. Relations (A.8) and (A.10) define the right hand sides of (71) for $\alpha = b$, i.e. for the image component representing the instantaneous homogeneous background.

A.2. Delayed point scatterer (*t*-scatterer) $\nu_t(t_z, z)$ in (55) and (56)

$$\nu(t_z, \mathbf{z}) = \nu_t(t_z, \mathbf{z}) = \mu_t(t_z) \delta(\mathbf{z} - \mathbf{z}_d), \quad \langle \overline{\mu_t(t_a)} \mu_t(t_b) \rangle = \sigma_t^2 F_t(Bt_a/2) \delta(t_a - t_b). \quad (\text{A.11})$$

Substituting (A.11) into (A.1) and (A.2), we obtain

$$I_t(\zeta_y, \eta_d, \xi_d) = N\tau \cdot \Phi(\eta_d, \kappa \xi_d) \int_0^\infty \mu_t(t_z) \exp\left(-2i \frac{\omega_0}{B} \zeta_d\right) \operatorname{sinc} \zeta_d dt_z \quad (\text{A.12})$$

where

$$\eta_d = k_{0\theta} \varphi_T(y_1 - z_{d1}), \quad \xi_d = \frac{Bk_{0\theta}}{\omega_0}(y_2 - z_{d2}), \quad \zeta_d = \xi_d + \zeta_y - \frac{Bt_z}{2}, \quad (\text{A.13})$$

and $\zeta_y = Bt_y/2$ as in (A.5). Note that unlike (44), dimensionless arguments of I_t in (A.12) are not aligned with the ambiguity lines, which can be expressed as ($\eta_d = \text{const}$, $\xi_d + \zeta_y = \text{const}$).

From (A.11) and (A.12), we can derive the following relations for expectations of the intensity and correlation along the ambiguity line:

$$\begin{aligned} \langle |I_t(\zeta_y, \eta_d, \xi_d)|^2 \rangle &= \sigma_t^2 \cdot N^2 \tau^2 \frac{2}{B} \check{F}_t(\zeta_y + \xi_d) \cdot |\Phi(\eta_d, \kappa \xi_d)|^2, \\ \langle \overline{I_t(\zeta_y, \eta_d, \xi_d)} I_t(0, \eta_d, \xi_d + \zeta_y) \rangle &= \sigma_t^2 \cdot N^2 \tau^2 \frac{2}{B} \check{F}_t(\zeta_y + \xi_d) \\ &\quad \cdot \Phi(\eta_d, \kappa(\xi_d + \zeta_y)) \overline{\Phi(\eta_d, \kappa \xi_d)}, \end{aligned} \quad (\text{A.14})$$

where

$$\check{F}_t(\zeta) \stackrel{\text{def}}{=} \int_0^\infty F_t(\zeta') \text{sinc}^2(\zeta - \zeta') d\zeta'. \quad (\text{A.15})$$

If we take $F_t(\zeta) = (1 + \text{sign}(\zeta))/2$ as in (57), or any other function F_t that slowly varies on the interval of $(\zeta - \pi, \zeta + \pi)$ for $|\zeta| \gtrsim \pi$, then $\check{F}_t(\zeta) \approx \pi F_t(\zeta)$ for $|\zeta| \gtrsim \pi$. Hence, the arguments of \check{F}_t in (A.14) can be understood as follows: scatterer (A.11) affects the image as long as $(\zeta_y + \xi_d) \gtrsim \pi$; in other words, the ambiguity line (see figure 3) drawn through (t_y, \mathbf{y}) should intersect the ray $\{(t'_y, \mathbf{y}') \mid \mathbf{y}' = \mathbf{z}_d; Bt'_y/2 > \pi\}$. At the same time, for $(\zeta_y + \xi_d) \lesssim -\pi$, the scatterer has no effect on the image, and the transition area width is of the order of range resolution.

With the help of the anti-derivative

$$\text{sinc}^2 \zeta = \left(\text{Si}(2\zeta) - \sin \zeta \text{sinc} \zeta \right)',$$

where $\text{Si}(\zeta) = \int_0^\zeta \text{sinc} \zeta' d\zeta'$ is the sine integral, we can calculate

$$\check{F}_t(\zeta) = \frac{\pi}{2} + \text{Si}(2\zeta) - \sin \zeta \text{sinc} \zeta$$

for the simple case when $F_t(\zeta)$ is the Heaviside function used in section 6. In order to normalize expressions (A.14), we take $\zeta \gg \pi$ in (A.15); this yields $\check{F}_t(\zeta) \approx \pi$. For the the right hand sides of (72)–(74), we are only interested in $\eta_d = 0$ and $\xi_d = 0$. Hence, for $\alpha = t$ in (71), we have the following expressions:

$$\begin{aligned} K_t &= N^2 \tau^2 \frac{2}{B} \pi, \quad G_t^S[F_t](\zeta) = \frac{1}{\pi} |\Phi(0, \kappa \zeta)|^2 \check{F}_t(\zeta), \\ G_t^T[F_t](\zeta) &= \frac{1}{\pi} \check{F}_t(\zeta), \quad H_t[F_t](\zeta) = \frac{1}{\pi} \Phi(0, \kappa \zeta) \check{F}_t(\zeta). \end{aligned} \quad (\text{A.16})$$

A.3. Inhomogeneous instantaneous scatterer (s-scatterer) $\nu_s(t_z, \mathbf{z})$ in (58) and (59)

$$\begin{aligned} \nu(t_z, \mathbf{z}) &= \nu_s(t_z, \mathbf{z}) = \delta(t_z) \delta(z_1 - z_{d1}) \mu_s(z_2 - z_{d2}), \\ \langle \overline{\mu_s(s_a)} \mu_s(s_b) \rangle &= \sigma_s^2 F_s(Bk_{0\theta} s_a / \omega_0) \delta(s_a - s_b). \end{aligned} \quad (\text{A.17})$$

Substituting (A.17) into (A.1) and (A.2) and using the notation $s = z_2 - z_{d2}$, we obtain

$$I_s(\zeta_y, \eta_d, \xi_d) = N\tau \int_0^\infty \mu_s(s) \exp\left(-2i\frac{\omega_0}{B}\zeta_0\right) \text{sinc } \zeta_0 \Phi(\eta_d, \kappa(\xi_d - \xi_s)) \, ds,$$

where

$$\xi_s = \frac{B}{\omega_0} k_{0\theta} s, \quad \zeta_0 = \frac{B}{\omega_0} k_{0\theta} (y_2 - z_2) + B \frac{t_y}{2} = \xi_d + \zeta_y - \xi_s,$$

see (A.4) and (A.13). Similarly to (A.14), we obtain for the s-scatterer the following relations:

$$\begin{aligned} \langle |I_s(\zeta_y, \eta_d, \xi_d)|^2 \rangle &= \sigma_s^2 \cdot N^2 \tau^2 \frac{\omega_0}{B k_{0\theta}} \\ &\quad \cdot \int_0^\infty |\Phi(\eta_d, \kappa(\xi_d - \xi_s))|^2 \text{sinc}^2(\xi_d + \zeta_y - \xi_s) F_s(\xi_s) \, d\xi_s, \\ \langle \overline{I_s(\zeta_y, \eta_d, \xi_d)} I_s(0, \eta_d, \xi_d + \zeta_y) \rangle &= \sigma_s^2 \cdot N^2 \tau^2 \frac{\omega_0}{B k_{0\theta}} \\ &\quad \cdot \int_0^\infty \Phi(\eta_d, \kappa(\xi_d + \zeta_y - \xi_s)) \overline{\Phi(\eta_d, \kappa(\xi_d - \xi_s))} \text{sinc}^2(\xi_d + \zeta_y - \xi_s) F_s(\xi_s) \, d\xi_s. \end{aligned} \quad (\text{A.18})$$

The argument of sinc^2 on the right sides of (A.18) implies that the inhomogeneous scatterer (A.17) affects the image as long as $(\xi_d + \zeta_y) \gtrsim \pi$ (see (A.14)).

In order to achieve a proper normalization of $G_s^{S,T}$, we use the same approach as for (A.14). Namely, consider the upper formula in (A.18) for $\zeta_y = 0$ and $\eta_d = 0$ when F_s is the Heaviside function (57). Shifting the integration variable, we reduce this formula to

$$\langle |I_s(0, 0, \xi_d)|^2 \rangle = \sigma_s^2 \cdot N^2 \tau^2 \frac{\omega_0}{B k_{0\theta}} \int_{-\xi_d}^\infty |\Phi(0, \kappa\zeta)|^2 \text{sinc}^2 \zeta \, d\zeta, \quad (\text{A.19})$$

where the dependence of the right hand side on y_2 is via ξ_d , see (A.13). When $\xi_d \gg 1$ (or, equivalently, $|y_2 - z_{d2}| \gg \Delta_R$), the integral on the right hand side does not depend on ξ_d , which is expected if we realize that the left hand side of (A.19) is the standard SAR image taken downrange by many resolution sizes with respect to the inhomogeneity at $z = z_d$ due to the s-target. We normalize this integral by its value at $\kappa = 0$, hence,

$$K_s = N^2 \tau^2 \frac{\omega_0}{B k_{0\theta}} \pi.$$

Taking $\eta_d = 0$ and $\xi_d = 0$ similarly to the case of t-scatterer, we obtain

$$\begin{aligned} G_s^S[F_s](\zeta) &= \frac{1}{\pi} \int_0^\infty |\Phi(0, \kappa(\zeta - \xi))|^2 \text{sinc}^2(\zeta - \xi) F_s(\xi) \, d\xi, \\ G_s^T[F_s](\zeta) &= \frac{1}{\pi} \int_0^\infty |\Phi(0, -\kappa\xi)|^2 \text{sinc}^2(\zeta - \xi) F_s(\xi) \, d\xi, \\ H_s[F_s](\zeta) &= \frac{1}{\pi} \int_0^\infty \Phi(0, \kappa(\zeta - \xi)) \overline{\Phi(0, -\kappa\xi)} \text{sinc}^2(\zeta - \xi) F_s(\xi) \, d\xi. \end{aligned} \quad (\text{A.20})$$

These expressions are used in (71) for $\alpha = s$.

A.4. Terms I_n in (66) and (69)

We have chosen the form of the noise term in (66) and (69) as $I_n(t, \mathbf{y})$ to achieve uniformity of notations for the image components in (71) and on. In the absence of any specific information

about the properties of the noise, we choose to define it as an uncorrelated additive term in (72)–(74), so there is no underlying reflectivity function $\nu(t, \mathbf{z})$ in (A.1) for I_n . In the notations of (71), we can formally set

$$G_n^{S,T}[F_n](\cdot) \equiv 1, \quad H_n[F_n](\cdot) \equiv 0, \quad K_n = 1,$$

but the only essential part is choosing the noise level $\sigma_n^2 K_n$: it is defined relative to the reflectivity of the homogeneous background $\sigma_b^2 K_b$ via the constant p_n , see (88). So, in order to implement the noise term in equations (66), we generate both I_n^S and I_n^T for (68) and (70) as uncorrelated pseudo-random circular Gaussian (as in (48) and (49)) numbers with the variance given by p_n .

ORCID iDs

Mikhail Gilman  <https://orcid.org/0000-0001-6970-627X>

References

- [1] Chen V C and Ling H 2002 *Time-Frequency Transforms for Radar Imaging and Signal Analysis* (Artech House Radar Library) (Norwood, MA: Artech House)
- [2] Medina R, Penn J and Albanese R 2002 Dielectric response data on materials of military consequence *Technical Report AFRL-HE-BR-TR-2002-0155*, United States Air Force Research Laboratory, Human Effectiveness Directorate, Directed Energy Bioeffects Division, Biomechanics and Modeling Branch, Brooks AFB, San Antonio, TX
- [3] Albanese R A and Medina R L 2013 Materials identification synthetic aperture radar: progress toward a realized capability *Inverse Problems* **29** 054001
- [4] Cheney M 2013 Imaging frequency-dependent reflectivity from synthetic-aperture radar *Inverse Problems* **29** 054002
- [5] Sotirelis P, Parker J, Hu X, Cheney M and Ferrara M 2013 Frequency-dependent reflectivity image reconstruction *SPIE Defense, Security and Sensing* (Bellingham, WA: International Society for Optics and Photonics) p 874602
- [6] Ferrara M, Homan A and Cheney M 2017 Hyperspectral SAR *IEEE Trans. Geosci. Remote Sens.* **55** 1–14
- [7] Goodman J W 1976 Some fundamental properties of speckle *J. Opt. Soc. Am.* **66** 1145–50
- [8] Goodman J W 1984 Statistical properties of laser speckle patterns *Laser Speckle and Related Phenomena* (Berlin: Springer) pp 9–75
- [9] Oliver C and Quegan S 1998 *Understanding Synthetic Aperture Radar Images* (Artech House Remote Sensing Library) (Boston, MA: Artech House)
- [10] Cumming I G and Wong F H 2005 *Digital Processing of Synthetic Aperture Radar Data. Algorithms and Implementation* (Boston, MA)
- [11] Cheney M and Borden B 2009 *Fundamentals of Radar Imaging* (CBMS-NSF Regional Conf. Series in Applied Mathematics vol 79) (Philadelphia, PA)
- [12] Gilman M, Smith E and Tsynkov S 2017 *Transionospheric Synthetic Aperture Imaging* (Applied and Numerical Harmonic Analysis) (Cham: Springer)
- [13] Borden B 1998 Dispersive scattering for radar-based target classification and duct-induced image artifact mitigation *NATO Symp. on Non-Cooperative Air Target Identification Using Radar* (North Atlantic Treaty Organization, Research and Technology Organization) pp 14.1–14.7
- [14] Beckmann P and Spizzichino A 1963 *The Scattering of Electromagnetic Waves from Rough Surfaces* (New York: Pergamon)
- [15] Gilman M A, Mikheev A G and Tkachenko T L 1996 A two-scale model and other methods for the approximate solution of the problem of diffraction by an uneven surface *Comput. Math. Math. Phys.* **36** 1429–42
- [16] Bass F G and Fuks I M 1979 *Wave Scattering from Statistically Rough Surfaces* (Oxford: Pergamon) (translated and ed C B Vesecky and J F Vesecky)

- [17] Elfouhaily T M and Guérin C-A 2004 A critical survey of approximate scattering wave theories from random rough surfaces *Waves Random Media* **14** R1–40
- [18] Gilman M and Tsynkov S 2015 A mathematical model for SAR imaging beyond the first Born approximation *SIAM J. Imaging Sci.* **8** 186–225
- [19] Moses R L, Potter L C and Cetin M 2004 Wide-angle SAR imaging *Defense and Security* (International Society for Optics and Photonics) pp 164–75
- [20] Chan T-K, Kuga Y and Ishimaru A 1999 Experimental studies on circular SAR imaging in clutter using angular correlation function technique *IEEE Trans. Geosci. Remote Sens.* **37** 2192–7
- [21] Moore L J and Potter L C 2007 Three-dimensional resolution for circular synthetic aperture radar *Defense and Security Symp.* (International Society for Optics and Photonics) p 656804
- [22] Kim A J, Fisher J W III and Willsky A S 2003 Detection and analysis of anisotropic scattering in SAR data *Multidimens. Syst. Signal Process.* **14** 49–82
- [23] Bleszynski E, Bleszynski M and Jaroszewicz T 2013 Autofocus algorithm for synthetic aperture radar imaging with large curvilinear apertures *Inverse Problems* **29** 054004
- [24] Varshney K R, Cetin M, Fisher J W III and Willsky A S 2006 Joint image formation and anisotropy characterization in wide-angle SAR *Defense and Security Sympos.* (International Society for Optics and Photonics) p 62370D
- [25] Gilman M, Smith E and Tsynkov S 2014 Single-polarization SAR imaging in the presence of Faraday rotation *Inverse Problems* **30** 075002
- [26] Garnier J 2016 Passive synthetic aperture imaging with limited noise sources *Inverse Problems* **32** 095008
- [27] NIST Digital Library of Mathematical Functions *Release 1.0.9 of 2014-08-29* <http://dlmf.nist.gov/>
- [28] Barrett H H and Myers K J 2004 *Foundations of Image Science* (New York: Wiley)
- [29] Lapidoth A 2017 *A foundation in Digital Communication* (Cambridge: Cambridge University Press)
- [30] Gallager R G 2008 *Principles of Digital Communication* vol 1 (Cambridge: Cambridge University Press)
- [31] Gallager R G 2008 Circularly-symmetric Gaussian random vectors Online at www.rle.mit.edu/rgallager/documents/CircSymGauss.pdf
- [32] Øksendal B 2003 *Stochastic Differential Equations. An Introduction with Applications* (Universitext) 6th edn (Berlin: Springer)
- [33] Holden H, Øksendal B, Ubøe J and Zhang T 2010 *Stochastic Partial Differential Equations. A Modeling, White Noise Functional Approach* (Universitext) 2nd edn (New York: Springer)
- [34] Lindgren G 2013 *Stationary Stochastic Processes: Theory and Applications* (Chapman & Hall/CRC Texts in Statistical Science Series) (Boca Raton, FL: CRC Press)
- [35] Fouque J-P, Garnier J, Papanicolaou G and Sølna K 2007 *Wave Propagation and Time Reversal in Randomly Layered Media* (Stochastic Modelling and Applied Probability vol 56) (New York: Springer)
- [36] Papoulis A 1984 *Probability, Random Variables and Stochastic Processes* (McGraw-Hill Series in Electrical Engineering. Communications and Information Theory) 2nd edn (New York: McGraw-Hill)
- [37] Allen J C and Hobbs S L 1997 Spectral estimation of non-stationary white noise *J. Franklin Inst.* **B 334** 99–116
- [38] Ulaby F T and Dobson M C 1989 *Handbook of Radar Scattering Statistics for Terrain* (Artech House Remote Sensing Library) (Norwood, MA: Artech House)
- [39] Trintinalia L C and Ling H 1997 Joint time-frequency ISAR using adaptive processing *IEEE Trans. Antennas Propag.* **45** 221–7
- [40] Canny J 1986 A computational approach to edge detection *IEEE Trans. Pattern Anal. Mach. Intell.* **PAMI-8** 679–98
- [41] Basu M 2002 Gaussian-based edge-detection methods—a survey *IEEE Trans. Syst. Man Cybern. C* **32** 252–60
- [42] Ziou D *et al* 1998 Edge detection techniques—an overview *Pattern Recogn. Image Anal. C/C Raspoznavaniye Obrazov I Analiz Izobrazhenii* **8** 537–59
- [43] Marr D and Hildreth E 1980 Theory of edge detection *Proc. R. Soc. Lond. B* **207** 187–217
- [44] Mendenhall W and Scheaffer R L 1973 *Mathematical Statistics with Applications* (North Scituate, MA: Duxbury Press)

- [45] Hastie T, Tibshirani R and Friedman J 2009 *The Elements of Statistical Learning: Data Mining, Inference, and Prediction (Springer Series in Statistics)* 2nd edn (New York: Springer)
- [46] Devaney A J 2012 *Mathematical Foundations of Imaging, Tomography and Wavefield Inversion* (Cambridge: Cambridge University Press)
- [47] Capozzoli A, Curcio C, Di Vico A and Lisenio A 2011 NUFFT- & GPU-based fast imaging of vegetation *IEICE Trans. Commun.* **94** 2092–103